

Determination of Lift Produced by 3D Printed Airfoils in a Wind Tunnel Through the Use of Manometers

By

Shreyas Krishnan, Taaseen Jahan, and Aaryan Mahipal

Team 2

Instructors: Professor Kamau Wright and Professor David Wooton

Experimental System Design Report for ME360

4/28/24

Table of Contents

Abstract.....	2
Introduction.....	3
Experimental Methods.....	4
Apparatus.....	4
Wind Tunnel Calibration.....	4
External Flow Characterization.....	5
Instrumentation.....	8
Wind Tunnel Calibration.....	8
External Flow Characterization.....	9
Procedure.....	9
Wind Tunnel Calibration.....	9
External Flow Characterization.....	10
Results.....	12
Wind Tunnel Calibration.....	12
External Flow Characterization.....	13
Discussion.....	16
Fundamental Theory.....	16
Calculations and Error Propagation.....	16
Force, Lift and Coefficient of Lift vs Speed.....	18
Varying Angle of Attack.....	23
Flaws in Data Collection.....	24
Experimental vs Theoretical.....	26
Conclusion.....	28
Bibliography.....	29
Appendix I: Problem Formulation Diagram.....	30
Appendix II: BOM.....	31
Appendix III: Design Drawings.....	33
Appendix IV: Wind Tunnel Calibration Data.....	36
Appendix V: Lift Calculation Data.....	38
Appendix VI: Theoretical Plots.....	56

ABSTRACT

The goal of the experiment was to develop an educational rig that characterizes the external flow of a 3D printed airfoil. A NACA2418 airfoil profile was used, and the lift produced as well as the coefficient of lift were calculated for various angles of attack. This was done by looking at pressure differences in manometers to measure pressure values at different pressure taps on the airfoil.

The wind tunnel was calibrated using an anemometer to determine the linear relationship between frequency of the wind tunnel and wind speed. Furthermore, the pressures measured at various points on the airfoil held a parabolic relationship with wind speed. This relationship was upheld as the angle of attack varied. A similar parabolic was obtained when the force was evaluated against varying wind speeds.

Experimental results implied that the lift also held a parabolic relationship with wind speed and as the angle of attack was increased, the lift produced by the airfoil also increased. This closely follows fluid dynamics theory. A similar trend was demonstrated by the coefficient of lift, which increased as the angle of attack was increased. The external flow characterization of the airfoil was conducted over five trials. Three of these trials were run using atmospheric pressure as a reference point for the manometer rig while two trials were run using the wind tunnel's dynamic pressure as a reference point for the manometer rig.

The experiment designed ultimately met client needs, delivering an experimental rig that can utilize the wind tunnel effectively providing students with a hands-on fluid dynamics learning experience characterizing external flow through lift and coefficient of lift calculations and hands-on experience with aerospace equipment.

INTRODUCTION

At The Cooper Union for the Advancement of Science and Art, engineering students do not get much experience with hands-on work in the aerospace field. There are multiple classes, such as fluid mechanics and aerodynamics, where students could benefit from fluids-related and aerodynamics-related experiments. Currently, there is a wind tunnel located in the LL224 that is underused and can serve as a great learning tool for the students. Knowledge of the wind tunnel and what it can be used for can prepare Cooper Union students for careers in the aerospace industry.

Our client, Professor Kamau Wright, would like an experiment that can be easily performed by students in fluid mechanics and aerodynamics. The experiment should make use of the wind tunnel and result in the students calculating the lift produced by airfoils designed and/or manufactured by the students. A 3D printed airfoil was used to design this experiment, which had a NACA 2418 profile. The experiment should also require students to physically adjust the angle of attack and directly read measurements as opposed to reading data from a computer. Near the wind tunnel in LL224 and in the reproduction of the wind tunnel section of 703, are a few attempts of manometer setups that would be used in conjunction with pressure taps on an air foil. These systems are not easy to set up and have height readings that are inaccurate in their measurements.

The goal was to develop an educational rig that makes use of manometers to measure pressure values at different points on a 3D printed airfoil with pressure taps and use this data to calculate the lift produced by the airfoil. This rig was easy to set up and to read the multiple height measurements and allows the students to calculate lift.

Manometers were used due to their simplicity and the fact that the theory behind the device is covered early in fluid mechanics. The manometer is easy to use and relies on manual data readings, and thus, it is the perfect device for students to interact with when using the wind tunnel. The formula needed to calculate lift is just an adaptation of principles learned in previous classes, and the formula needed for the lift coefficient is new but simple. This would expose students to a fundamental aerodynamic concept in a clear and simple way.

EXPERIMENTAL

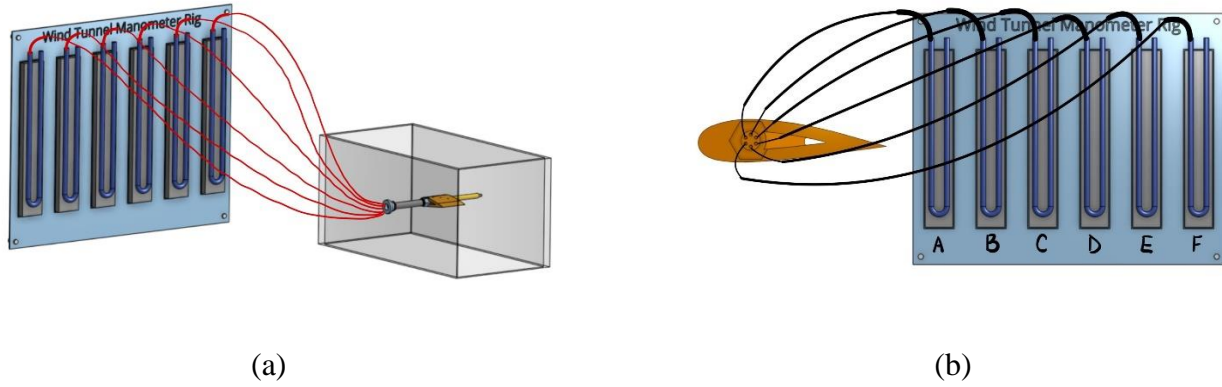


Figure 1. (a) 3D and (b) 2D images of the experimental system displaying the use of manometers with the pressure taps of a NACA 2418 airfoil.

Apparatus

Wind Tunnel Calibration

The test section of the wind tunnel is an empty box with a few removable plexiglass plates that can be used for mounting prototypes and instrumentation. Since anemometers were to be used for collecting velocity data, it was necessary that the apparatus extended the instrument toward the middle of the test section and was adjustable such that the anemometer could be oriented to face the direction of the oncoming wind. This was done by repurposing a soldering clamp stand.

The shaft was unscrewed from the base of the stand and constrained one of the removable plates with an M6 screw. Existing holes on the plates made this easy to accomplish and one of the holes fortunately positioned the shaft close to the center of the test section. Then, the clamps were used to hold the anemometer fan perpendicular to the direction of the wind. It was confirmed that the screen of the anemometer was also clearly visible from outside of the test section. The apparatus is shown here:



Figure 2. An anemometer mounted in the wind tunnel test section using apparatus.

After calibrating the wind tunnel a few times, a blip in the linear trend was noticed. Initially assumed to be a power loss at specific frequencies, the blip was eliminated by replacing the anemometer with a new, updated anemometer. The apparatus setup with the new anemometer is shown below:



(a)

(b)

Figure 3. The Wintact Digital Anemometer mounted in the wind tunnel test section using apparatus.

The new anemometer eliminated the blip, establishing a linear relationship between the velocity and wind speed, therefore successfully calibrating the wind tunnel.

External Flow Characterization

To characterize the external flow, pressure data was to be collected from multiple points across an airfoil. While the anemometers could be easily mounted using the above detailed apparatus, mounting an airfoil required a new apparatus that could constrain to the airfoil's hexagonal mounting hole and accommodate the hypodermic needles protruding from the opposite side. These needles would connect the surface cavities and internal channels of the airfoil to PVC tubes that would connect to manometers that report the pressure at each of the 6 different cavities.

Before designing a secure and stable mount, the NACA 2418 airfoil was chosen for the entirety of the experiment. This airfoil was chosen because it was used in previous Fluid Mechanics classes at The Cooper Union and prior art relating to the wind tunnel make use of the same airfoil. Thus, a 3D-printed resin airfoil was already manufactured and could be physically used to create the design. By sizing down the NACA 2418, the airfoil had a chord of 4.171 inches and a span of 3.012 inches.

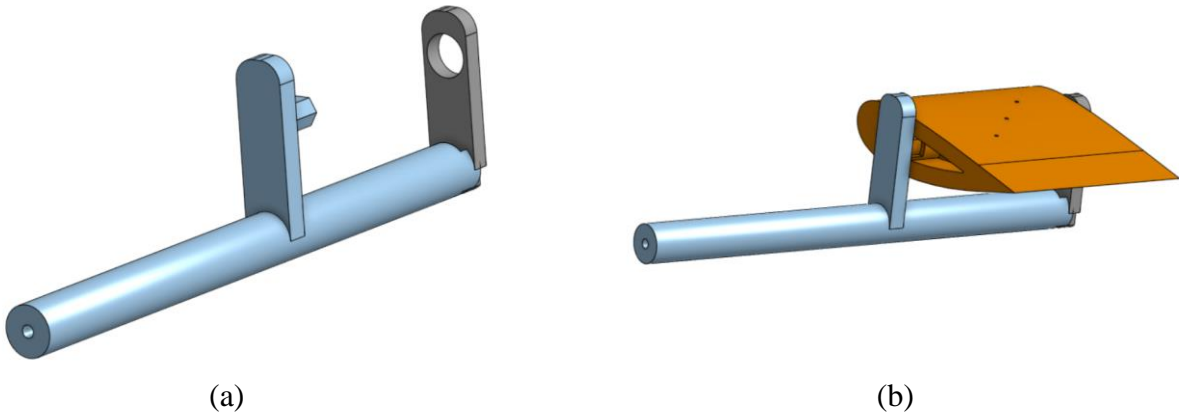


Figure 4. CAD images of the first airfoil mount prototype (a) without and (b) with the airfoil attached.

The first prototype for the airfoil mount is shown above, created entirely out of PLA using Prusa Mini 3 3D printers. The longer end of the shaft would have a tapped hole so that it could be mounted to the removable plates of the test section in a similar fashion to how the solder clamp stand was constrained. This hole extends through the entire shaft so that the gray part can be screwed tight against the airfoil. This would make sure that the airfoil was being pressed against the hexagonal extrusion. The gray part is removable and let hypodermic needles to pass through. The entire length of the mount is just over 6 inches so that it could be mounted in the middle of the test section's 12-inch depth.

The first prototype was successful in holding the airfoil centered within the wind tunnel, but upon further inspection, some flaws were identified. For example, the part of the mount underneath the airfoil would affect the pressure readings collected at the bottom pressure taps of the airfoil. This would skew the data and result in inaccurate lift calculations. Furthermore, mounting the airfoil on only one side of the wind tunnel causes there to be a moment induced by the wind and could result in the 3D-printed mount failing. Lastly, the tubing leading to the pressure taps would be exposed in the first prototypes and could result in the hypodermic needles being removed from the pressure channels. To address all these issues, a second prototype was designed.

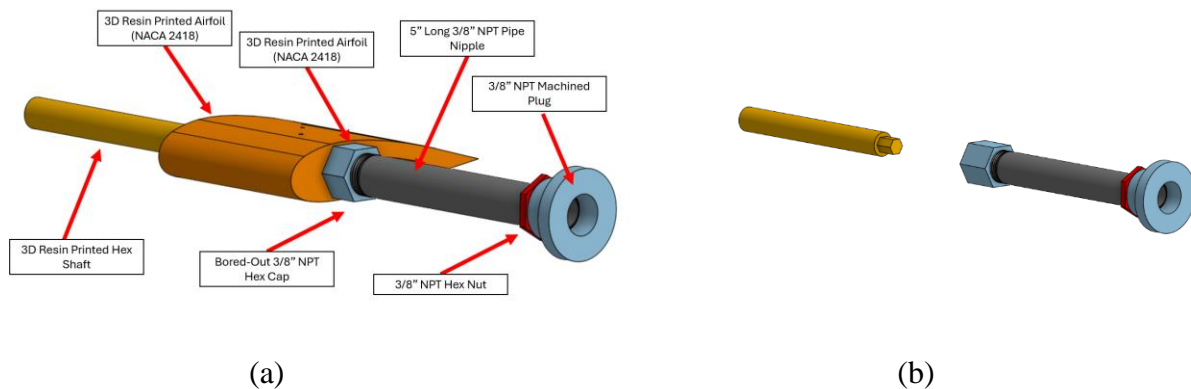


Figure 5. CAD images of the second airfoil mount prototype (a) with and (b) without the airfoil attached

In the second prototype, the 3D-printed hex shaft was kept, but instead only mounted to one side of the airfoil. It was also printed using Formlabs' resin 3D printer for extra durability and quality. Like the first prototype, the other end of the hex shaft was tapped and mounted to the wind tunnel glass using a 1/4-20 screw. To remove the moment induced in the first prototype, the second prototype mounts the other end of the airfoil with a 3/8" NPT threaded hex cap and a 5 inch long, 3/8" NPT nipple. The airfoil was modified to include a groove for the hex cap to fit into and the hex cap itself was bored out to have a through-hole for the tubing to pass through. The pipe nipple was then screwed into the hex cap. To constrain the pipe against the door of the wind tunnel test section, a different door was chosen that had a hole in the center that was larger than the diameter of the pipe. By machining a plug for the hole in the door that the pipe could screw into, the final design of the prototype mounted the airfoil in the middle of the test section with minimal edits to the airfoil itself. A CAD drawing of the NPT plug is shown in *Appendix III*.

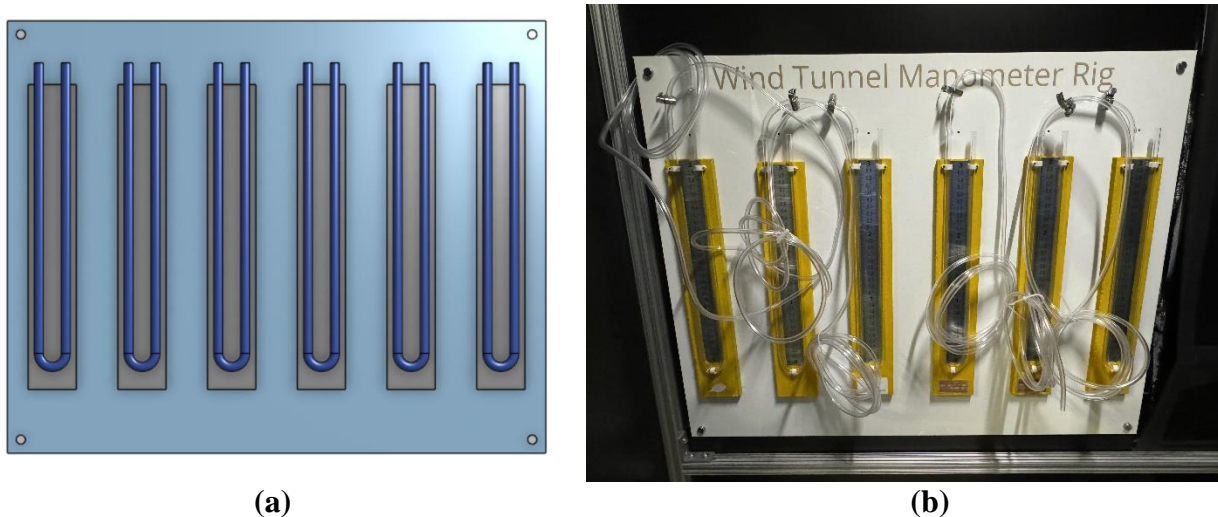


Figure 6. (a) CAD of 6-Manometer apparatus for manual data collection of pressure at 6 different surface cavities of airfoil, (b) Final Manometer Rig setup inside the wind tunnel mounted on the wall adjacent to the test section

The above image demonstrates the proposed apparatus for collecting pressure data. Each of the manometers would have one end of the tube connected to PVC tubes that would extend to smaller tubes attached to the endodermic needles that would be inserted into the pressure channel holes on the side of the airfoil. Hose clamps would tighten the PVC tubes over the manometer tubes. The manometers themselves are screwed onto an acrylic plate from the back. The entire setup would be mounted to a wall near the test section using stand-offs on each corner of the plate.

The airfoil mount and the manometer setup were to work in tandem such that students could rotate the airfoil, changing the angle of attack, and collect pressure data at each cavity of the airfoil using the manometers. Prior to the experiment, the students would set the wind tunnel to a desired speed, determined by using the wind calibration data.

Instrumentation

Wind Tunnel Calibration

The wind tunnel was calibrated to understand the relationship between frequency and wind speed, while taking note of uncertainties and instrumental errors in the wind tunnel itself. This allowed us to obtain a comprehensive set of standardized data which will be useful for calculating lift and drag, as well as finding sources of error. A set of two digital anemometers were used to measure the velocity of the wind over several sets of trials. The increments between each successive trial were changed after each complete set. The range and estimated uncertainty of each anemometer is shown in Table 1.

Table 1. Instrumental uncertainty and air velocity range for each measurement device used to calibrate the wind tunnel.

Instrument	Model	Air Velocity Range	Uncertainty
HTI Digital Anemometer	AO-HT-81	1.00 - 25.00 m/s	$\pm (3\% + 0.20 \text{ m/s})$
Wintact Digital Anemometer	WT8907	0.00 - 45.00 m/s	$\pm (3\% + 0.10 \text{ m/s})$

The Wintact anemometer has a much wider air velocity range and is equipped with a wind speed data logger. The wider air velocity range is necessary since wind tunnel max speeds are tested and those max speeds are outside the range of the HTI anemometer. This new anemometer allows for more accurate data readings in the upper range of air speeds. Therefore, the latter is the preferred instrument to use.



Figure 7. List and images of instrumentation devices. (a) HTI Digital Anemometer, and (b) Wintact Digital Anemometer

External Flow Characterization

The only instrumentation required for characterizing the external flow is a manometer with a range wide enough to measure the pressure induced by the wind tunnel at each of the surface cavities of the airfoil. The chosen manometer is shown below and has an adjustable zero. The uncertainty associated with the instrument is ± 0.005 KPa and the measurable pressure range is between 0 and 3 KPa.



Figure 8. 0-3 Kpa U-shaped manometers used to record pressure data.

To measure the change in the angle of attack, an inclinometer was used. The exact device we used is the GemRed 82413 Digital Angle Gauge Inclinometer. This device was zeroed with the flattest part of the trailing edge of the airfoil and the angle of attack changes were made with respect to that location. This device has an error of ± 0.05 deg but has an error of ± 0.15 deg while resting.



Figure 9. 0-3 GemRed Inclinometer used to measure angle of attack.

Procedure

Wind Tunnel Calibration

To calibrate the wind tunnel, an anemometer, a device used to measure air speed, was needed. This device needed to be securely mounted inside the wind tunnel so that it would not fly off and destroy the blades, and so that accurate measurements could be taken. The blades of the

anemometer had to be perpendicular to the air flow direction to ensure that the anemometer was taking accurate measurements. This requirement also ensures the repeatability of the data, so that data is not taken at an odd angle and directly compared with this data. Before acquiring the new and higher range anemometer, the anemometers found throughout the building were attempted. The first anemometer had a long neck, which allowed it to be clamped while another anemometer was just a rectangular prism and as a result could not be clamped.

First the anemometer needs to be attached to a rod clamp, which can be seen in *Figure 2*. The rod clamp was then attached to a long metal rod that was long enough to hold the anemometer in the center of the wind tunnel. The rod used a m6 screw. Along with a washer, this screw was inserted through the acrylic side panel of the wind tunnel and screwed into the rod. This whole setup can be seen in *Figure 2*.

Next, the necessary safety precautions need to be addressed before powering on the wind tunnel. First, there cannot be anyone or anything at the inlet and outlet of the wind tunnel. Next, the door to the lab needs to be shut. Most importantly, everyone in the lab needs to be wearing ear protection and the people directly using the wind tunnel need to be wearing eye protection. Finally, anything inside the wind tunnel needs to be secured so that it does not break the blades. After these rules have been followed, the wind tunnel can be powered on with a button. This will not generate any air speed; it just turns the machine on. To increase the air speed, there is a knob which is turned. This knob controls the frequency, from 0 Hz to 60 Hz. As one person controls the knob to increment the frequency values, another student should read the anemometer reading and the third student should record this data. This procedure allows for a calibration curve that clearly relates the frequency values on the machine directly to air speed values produced by the machine. This data is necessary since it will be used to determine the lift coefficient.

External Flow Characterization

Sample Student Procedure

To run the experiment, the airfoil was mounted in the wind tunnel's test section securely using the airfoil mount (Refer to *Figure 5*). This involved a few steps to ensure proper attachment. First, the right wind tunnel test section door was installed. Next, the window plug was inserted, and the hex nut was screwed all the way on to one side of the NPT nipple. The same end of the nipple was screwed into the window plug. The hex cap was screwed on the opposite end of the nipple. The other end of the airfoil was attached to a resin printed hex shaft which was screwed onto the removable circular test section with 1/4-20 screw, it is important to ensure that each connection was secure, and nothing would detach and damage the wind tunnel. Next, the hypodermic needles were connected to each individual airfoil channel, leading out through the NPT nipple, and eventually connecting the airfoil channels to the manometer rig. This in turn, securely mounted the airfoil onto the hex cap. After securing all the tubing, the test section is ready for the experiment. Before powering on the wind tunnel, the necessary safety procedures were repeated as described in the previous section. The wind tunnel is then powered on, and the following steps are repeated until 60Hz is reached.

The initial height difference in the manometer is recorded and the wind tunnel is set to 5 Hz frequency by rotating the knob on the power control. After recording the new height difference in the manometers, the procedure is repeated with 5 Hz increments until the last set of values are recorded at 60 Hz. The difference in liquid's height in the manometers and the wind speed

(calibrated earlier), are used to determine the force of lift and lift coefficients at different wind speeds.

A similar procedure was repeated after changing the wind's angle of attack on the airfoil. The angle of attack can be defined as the incidence angle of the chord line with respect to the free-stream velocity, where the chord line refers to an imaginary line connecting the leading and trailing edges of the airfoil. To accurately change the angle of attack, the wind tunnel test section is opened from the rear end by removing the circular disc carefully. A digital protractor can be placed on the flat surface of the trailing edge while rotating the airfoil around the resin printed hex shaft. This will allow us to change the angle of attack accurately. Once done, the circular disk is reattached to the test section window, and it is ensured that none of the tubing connected to the hypodermic needles have protruded outwards.

RESULTS

Wind Tunnel Calibration

Two trials were conducted to calibrate the wind speed of the wind tunnel. Since the wind tunnel has range of 0-60 Hz for its wind speed settings, the first trial consisted of recording the wind velocity using the anemometer for every 5 Hz. During the second trial, two sets of data were collected, one in which the speed was collected for every 2 Hz, and the other set for every 5 Hz. Both of these trials were conducted using the HTI Digital Anemometer. The data for 2 Hz increments are similar for both trials so only results for the second trial will be detailed here but graphs from trial 1 can be found in *Appendix IV*.

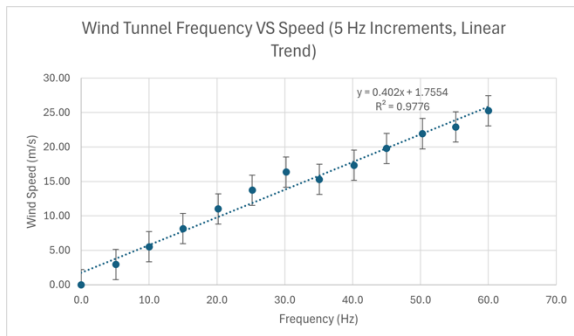


Figure 10. Graph of wind tunnel calibration curve for 5 Hz intervals with a linear fit applied.

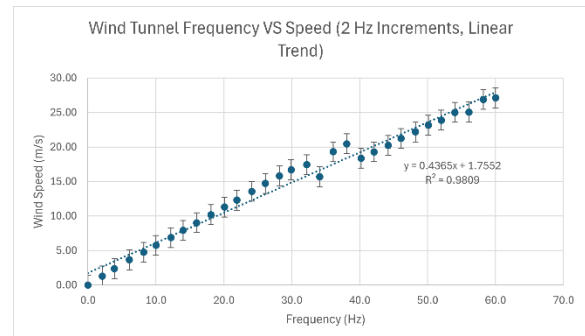


Figure 11. Graph of wind tunnel calibration curve for 2 Hz intervals with a linear fit applied.

As seen in the graphs above, both sets of data exhibit linear trends and this is supported by the high R-squared values. These values can also be compared against the polynomial curves of best fit graphs found after this paragraph. Since the polynomial trends have higher R-squared values it seems reasonable to assume that the relationship between the frequencies and the speeds are polynomial. However, it is likely that this is a skewed result due to graphs being inconsistent between 30 and 40 Hz.

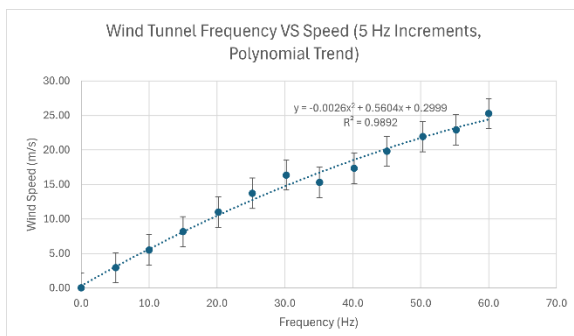


Figure 12. Graph of wind tunnel calibration curve for 5 Hz intervals with a polynomial fit applied.

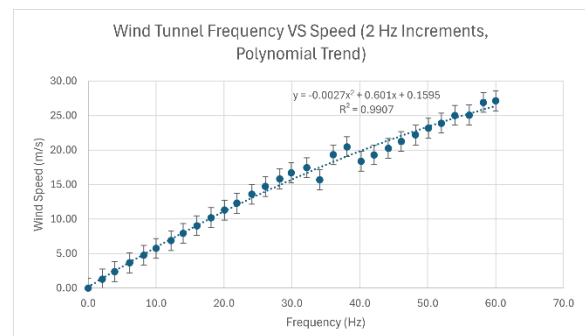


Figure 13. Graph of wind tunnel calibration curve for 2 Hz intervals with a polynomial fit applied.

Originally, data for 5 Hz intervals was collected first, which was when the inconsistency was first determined. To understand a clearer range at which the inconsistency occurred, the data for the 2 Hz intervals were collected. It is with this data that there is not only one but two drops in velocity between the 30 Hz and 40 Hz intervals. These drops occur at 34.1 Hz (15.68 m/s) and 40.2 Hz (18.37 m/s). During these tests the behavior of the wind tunnel was also analyzed, and it was noted that at around a frequency of 38.1 Hz (20.45 m/s), the wind tunnel loses power and then quickly starts spinning its fan again. It is possible that gradually increasing the frequency over a short period time causes the wind tunnel to fluctuate its power, causing the fluctuations at these frequencies. It was seen though that when decreasing frequency, there was no hysteresis present. Although the data indicates that the wind tunnel is to blame for the inconsistencies, it was also hypothesized that the anemometer range could be insufficient or deteriorated over time. Thus, the Wintact anemometer was ordered to run more tests and collect a new set of data.

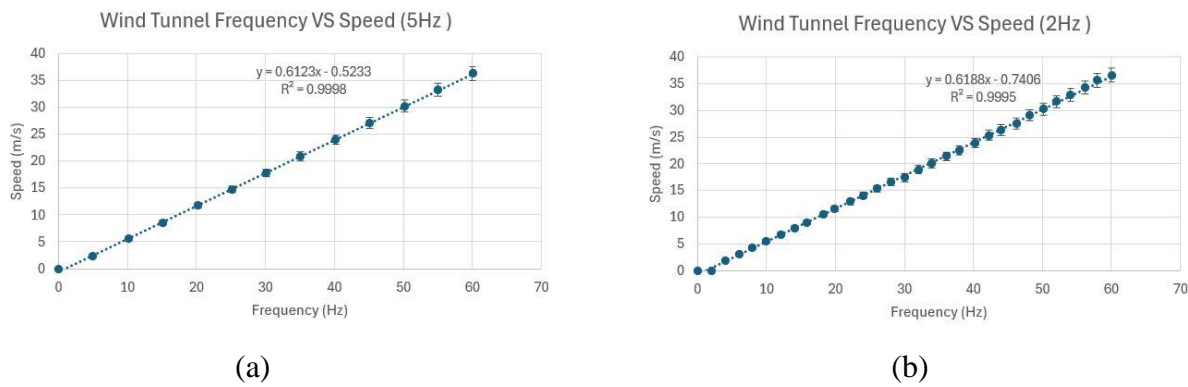


Figure 14. Graph of wind tunnel calibration curve using Wintact Digital Anemometer for (a) 5 Hz intervals and (b) 2 Hz intervals with a linear fit applied.

Two sets of data were collected with the new Wintact Digital Anemometer (refer to *Figure 3* for setup), at 5 Hz and 2 Hz intervals. This data fit perfectly into a linear trend with an R^2 value very close to 1. The inconsistencies in data no longer appeared.

External Flow Characterization

With the airfoil mounted securely in the wind tunnel, pressure values were collected for each pressure tap at different frequencies of the wind tunnel. Data was collected from 0-60 hertz in 5 hertz intervals. Using the linear fit equation from the wind calibration test conducted in 2 hertz intervals using the Wintact anemometer, the frequencies of the wind tunnel were converted to speeds and the pressures at each tap were plotted against the calculated speeds. For every plot forward, the speeds were converted the same way. The following figure depicts the pressure data collected for the first trial where the angle of attack was 0 degrees.

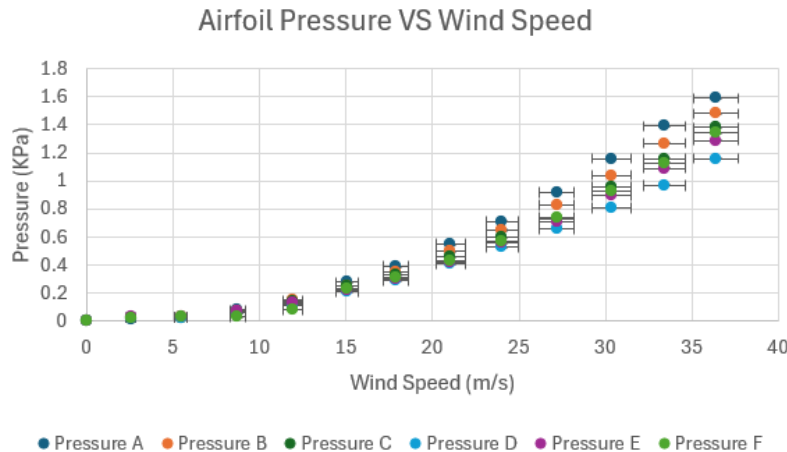


Figure 15. All pressure taps pressure vs wind speed.

In the above figure, error bars are displayed for both the speeds, calculated through error propagation, and the instrumental error associated with the pressure. The pressure error bars are not visible because the instrumental error is too small to be seen in the graph. The error associated with speeds is a percentage error, and as a result, the error increases as the wind speed increases. As seen in the figure, the trends for each pressure tap are largely the same so analyzing the relationship between one pressure tap and speed is sufficient. In the following figure, the pressure data collected for pressure tap A is plotted against speed for the same trial. Plots for the other individual pressure taps for each trial can be found in *Appendix V*.

Pressure A VS Wind Speed

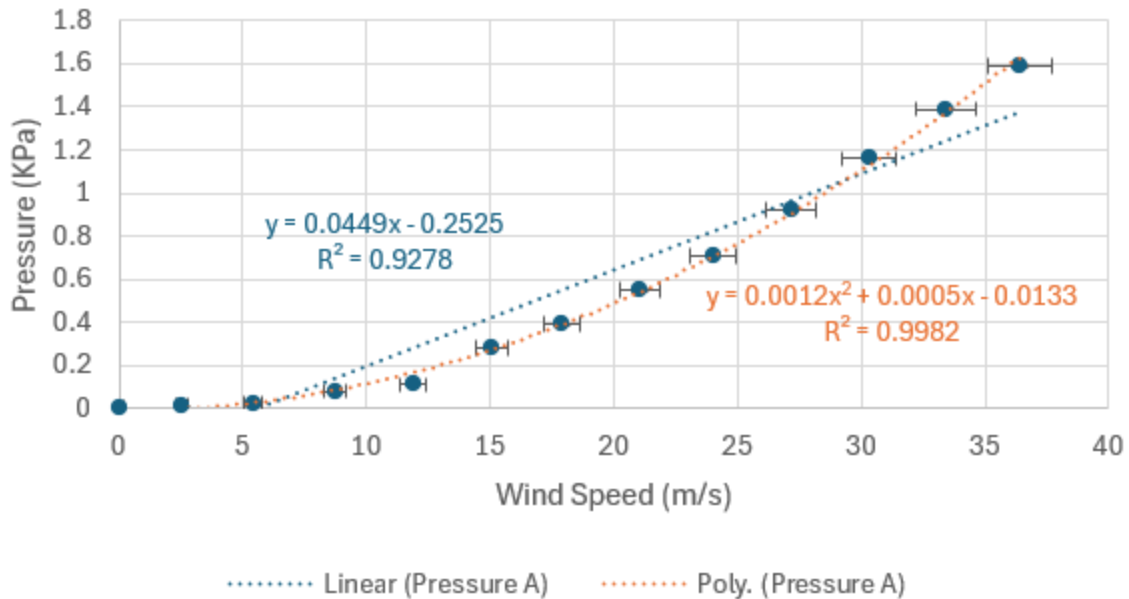


Figure 16. Pressure at pressure tap A vs wind speed

Figure 16 demonstrates both a linear and polynomial of order 2 curves of best fit applied to the data for pressure tap A. By looking at the R-squared values, it was concluded that the pressures along the airfoil had a parabolic relationship with the wind speed. It is likely that this is due to the design of the NACA 2418 airfoil. By looking at the pressure data for other angles of attack in Appendix V, the parabolic relationship still holds as the angle of attack is increased.

DISCUSSION

Fundamental Theory

Once all the data has been collected, the data can be processed to calculate the lift produced by the airfoil at different wind tunnel speeds and the coefficient of lift of the airfoil at its angle of attack can be determined.

The use of the manometers in this experiment allows for manual readings of pressure values which is a feature that our client wanted. Manual measurements allow for a more hands-on learning experience which would reinforce the concepts they learn from this experiment. The pressure readings that are read from the manometers are the pressure readings at the pressure taps on the airfoil. The pressure readings can be directly related to the force on the airfoil in that region of the airfoil. The pressure along the airfoil is a continuous curve and the pressure taps on the airfoil measure three specific pressure values along this curve. This allows for an approximation of the area under the pressure curve by use of a Riemann sum with three intervals. Since there are six pressure taps, the top side of the airfoil and bottom side of the airfoil each have their own approximations. To increase the accuracy of the experiment, an ideal setup would include an infinite number of pressures taps along the profile of the airfoil to increase the resolution of the Riemann sum. Using the relationship between force, pressure, and area, the forces can be calculated as well as the overall lift. In turn, using the wind speed and air conditions within the wind tunnel, the lift coefficient of the airfoil can be determined.

The calibration of the wind tunnel was necessary due to the need to relate wind tunnel control frequencies directly of air speed inside the wind tunnel. The air speeds are necessary to calculate the coefficient of lift. The frequency vs air speed data for this wind tunnel was not accessible and inaccurate. As a result, we created our own relationship between frequency and air speed using the anemometer so that we can calculate the coefficient of lift as accurately as possible.

Calculations and Error Propagation

The first step of the calculations was relating the pressure data collected from the manometers to force values. This makes use of the fundamental definition of pressure as shown in [Eq. 1].

$$P = \frac{F}{A} \quad [\text{Eq. 1}]$$

Since the theory of this experiment relies on the use of Riemann Sum, the area associated with the force at each pressure value is 1/3 of the total area of one side for each of the three taps on that side. Breaking down the area into length and width made it easier to define a flat rectangle as the surface of the top and bottom portions of the airfoil. Thus, [Eq. 2] substitutes the area for the product of the length and width of the airfoil divided by 3 for the area corresponding to each tap.

$$F = PA = \frac{Plw}{3} \quad [\text{Eq. 2}]$$

Once the forces at each pressure tap were calculated, a force balance was implemented to calculate the overall lift.

$$F_{lift} = F_{bottom} - F_{top} \quad [\text{Eq. 3}]$$

By designating the pressure taps on the top of the airfoil as A-C and the bottom pressure taps as D-F, [Eq 4] was derived. As seen in [Eq. 4], forces A-C are downwards while forces D-F are upwards since pressure acts perpendicular to the airfoil.

$$F_{lift} = [F_D + F_E + F_F] - [F_A + F_B + F_C] \quad [\text{Eq. 4}]$$

Thus, the definitions for pressure and area could be substituted into [Eq. 4] to derive [Eq. 5] and [Eq. 6].

$$F_{lift} = [P_D A_D + P_E A_E + P_F A_F] - [P_A A_A + P_B A_B + P_C A_C] \quad [\text{Eq. 5}]$$

$$F_{lift} = \frac{1}{3}[P_D lw + P_E lw + P_F lw] - \frac{1}{3}[P_A lw + P_B lw + P_C lw] \quad [\text{Eq. 6}]$$

With the overall lift force calculated, it could then be used with the total area of one side of the airfoil, the air density of the wind tunnel, and the wind speed to determine the coefficient of lift. [Eq. 7] demonstrates this and [Eq. 8] rearranges [Eq. 7] to solve for the coefficient of lift.

$$F_{lift} = \frac{1}{2} \rho v^2 C_l A \quad [\text{Eq. 7}]$$

$$C_l = \frac{2F_{lift}}{\rho v^2 A} = \frac{2F_{lift}}{\rho v^2 lw} \quad [\text{Eq. 8}]$$

Since each equation laid out above has an associated error due to instrumental uncertainty, error propagation was done using the Root Sum Square method. For [Eq. 2], the length and width of the airfoil was uncertain due to the accuracy of the FormLabs' resin 3D printer. Furthermore, the pressure data from the manometers had their own instrumental uncertainty. With these sources of error in mind, the error propagation for force calculations was setup as [Eq. 9].

$$\sigma_F = \sqrt{\left(\frac{\partial F}{\partial P}\right)^2 \sigma_P^2 + \left(\frac{\partial F}{\partial l}\right)^2 \sigma_l^2 + \left(\frac{\partial F}{\partial w}\right)^2 \sigma_w^2} \quad [\text{Eq. 9}]$$

[Eq. 10] was derived by making the necessary partial differentiation for [Eq. 9] using [Eq. 2].

$$\sigma_F = \sqrt{\left(\frac{lw}{3}\right)^2 \sigma_P^2 + \left(\frac{pw}{3}\right)^2 \sigma_l^2 + \left(\frac{pl}{3}\right)^2 \sigma_w^2} \quad [\text{Eq. 10}]$$

The next part of the calculations was the force balance in [Eq. 6] to calculate overall lift. The error propagation was set up to be [Eq. 11] as shown below and [Eq. 12] was created after making the necessary partial differentiations to [Eq. 6]. [Eq. 11] and [Eq. 12] also factor in the uncertainty values calculated for each force using [Eq. 10].

$$\sigma_{F_{lift}} = \sqrt{\left(\frac{\partial F_{lift}}{\partial F_D}\right)^2 \sigma_{F_D}^2 + \left(\frac{\partial F_{lift}}{\partial F_E}\right)^2 \sigma_{F_E}^2 + \left(\frac{\partial F_{lift}}{\partial F_F}\right)^2 \sigma_{F_F}^2 + \left(\frac{\partial F_{lift}}{\partial F_A}\right)^2 \sigma_{F_A}^2 + \left(\frac{\partial F_{lift}}{\partial F_B}\right)^2 \sigma_{F_B}^2 + \left(\frac{\partial F_{lift}}{\partial F_C}\right)^2 \sigma_{F_C}^2}$$

[Eq. 11]

$$\sigma_{F_{lift}} = \sqrt{\sigma_{F_D}^2 + \sigma_{F_E}^2 + \sigma_{F_F}^2 + \sigma_{F_A}^2 + \sigma_{F_B}^2 + \sigma_{F_C}^2}$$

[Eq. 12]

Since the last part of the calculations was determining the coefficient of lift using the overall lift force, velocity, and dimensions of the airfoil, [Eq. 13] demonstrates the error propagation that was used. Since there was uncertainty for the wind tunnel calibration data due to the instrumental uncertainty of the Wintact anemometer, this error was factored in along with the error associated with the FormLabs' resin 3D printer.

$$\sigma_{C_l} = \sqrt{\left(\frac{\partial C_l}{\partial F_{lift}}\right)^2 \sigma_{F_{lift}}^2 + \left(\frac{\partial C_l}{\partial v}\right)^2 \sigma_v^2 + \left(\frac{\partial C_l}{\partial l}\right)^2 \sigma_l^2 + \left(\frac{\partial C_l}{\partial w}\right)^2 \sigma_w^2}$$

[Eq. 13]

By making the necessary partial differentiation to [Eq. 13], [Eq. 14] was derived.

$$\sigma_{C_l} = \sqrt{\left(\frac{2}{\rho v^2 l w}\right)^2 \sigma_{F_{lift}}^2 + \left(\frac{-4 F_{lift}}{\rho v^3 l w}\right)^2 \sigma_v^2 + \left(\frac{-2 F_{lift}}{\rho v^2 l^2 w}\right)^2 \sigma_l^2 + \left(\frac{-2 F_{lift}}{\rho v^2 l w^2}\right)^2 \sigma_w^2}$$

[Eq. 14]

Force, Lift, and Coefficient of Lift VS Speed

Using the calculations of the lift forces, lift coefficients, and error propagations, graphs were generated that visually show the relationships between these values and the air speeds in the wind tunnel.

Figure 17 shows Forces vs Wind Speed for trial 1, which is the trial for a zero-degree angle of attack. Each data point has its associated error bars. The vertical error bars are present, but the vertical error is very small and as a result, the vertical error bars are not visible. The remaining plots of Forces vs Wind Speed for the other trials can be found in *Appendix V*.

Forces VS Wind Speed

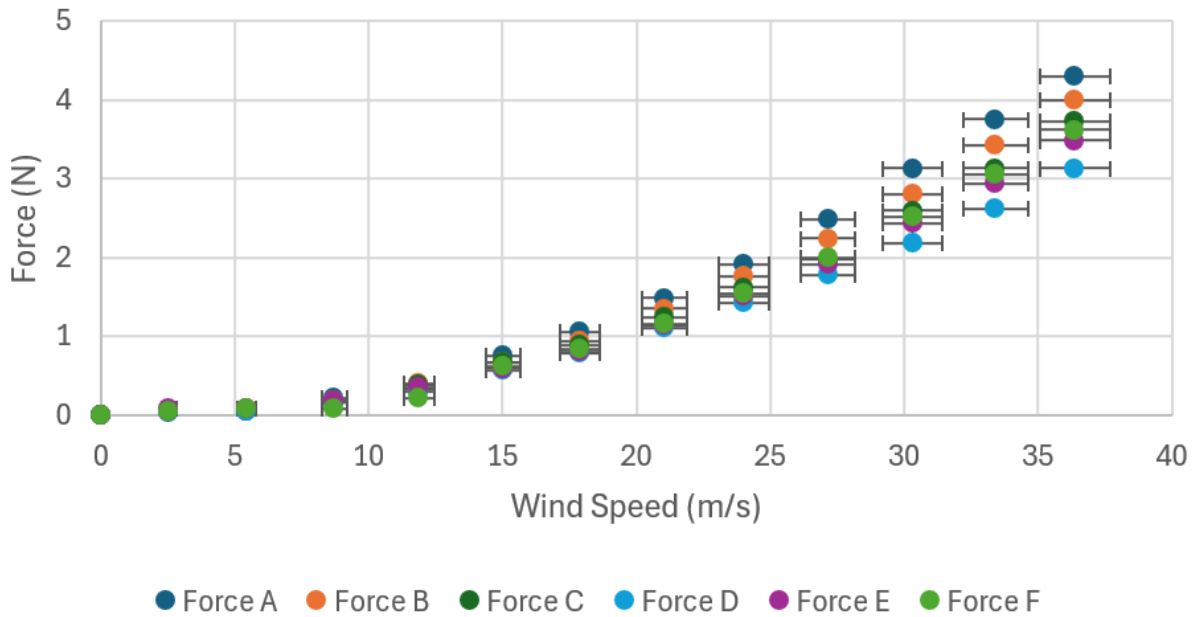


Figure 17. Force vs Wind Speed for zero-degree angle of attack with error bars

As seen by the graph above, the forces at each pressure tap followed a similar trend as the speed of the wind increased. While at low speeds, the forces were fairly the same at each pressure tap, the trend for each force begins to deviate from each other at higher speeds. The graph also demonstrates how forces A and D, B and E, and C and F are related to each other. The difference between forces A and D are the largest while the difference between forces C and F are the smallest. This is due to the locations of the pressure taps on the airfoil since D is directly underneath A, E underneath B, and F underneath C. The difference between forces C and F are the smallest because the pressure taps at these locations are closest to the trailing edge.

Since the forces follow similar trends, the graph for one of the forces plotted against wind speed was analyzed to determine the type of correlation that exists between force and speed. The graph for the force at pressure tap A versus wind speed is shown below in *Figure 18*. Appendix V contains the graphs for each of the other forces plotted against wind speed.

Force A VS Wind Speed

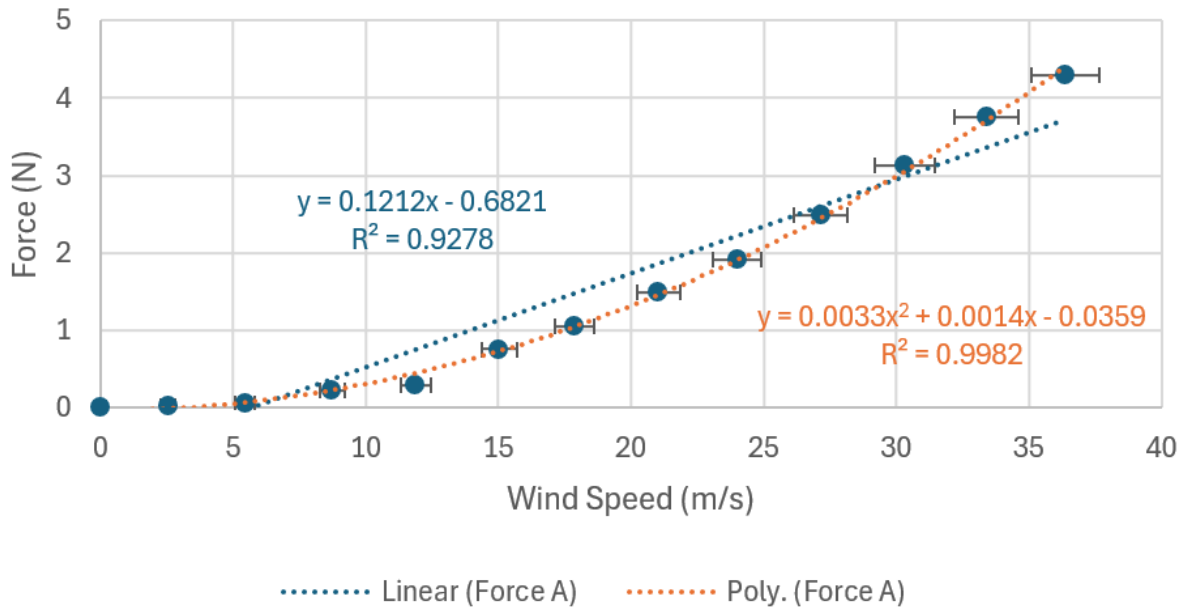


Figure 18. Force A vs Wind Speed for zero-degree angle of attack with error bars.

The graph above shows how when the data is overlayed with a linear fit and a polynomial fit of order 2, the polynomial fit has a greater R-squared value. This indicates that the relationship between force and wind speed of the airfoil is parabolic. Again, the error propagation done for this portion of the calculations proved that the error associated with forces is small. Thus, the vertical error bars for force cannot be seen. Using a force balance, the forces at all the pressure taps can be appropriately summed to calculate the force of lift on the airfoil. As such, *Figure 19* relates the overall lift force to the wind speed.

Lift VS Wind Speed

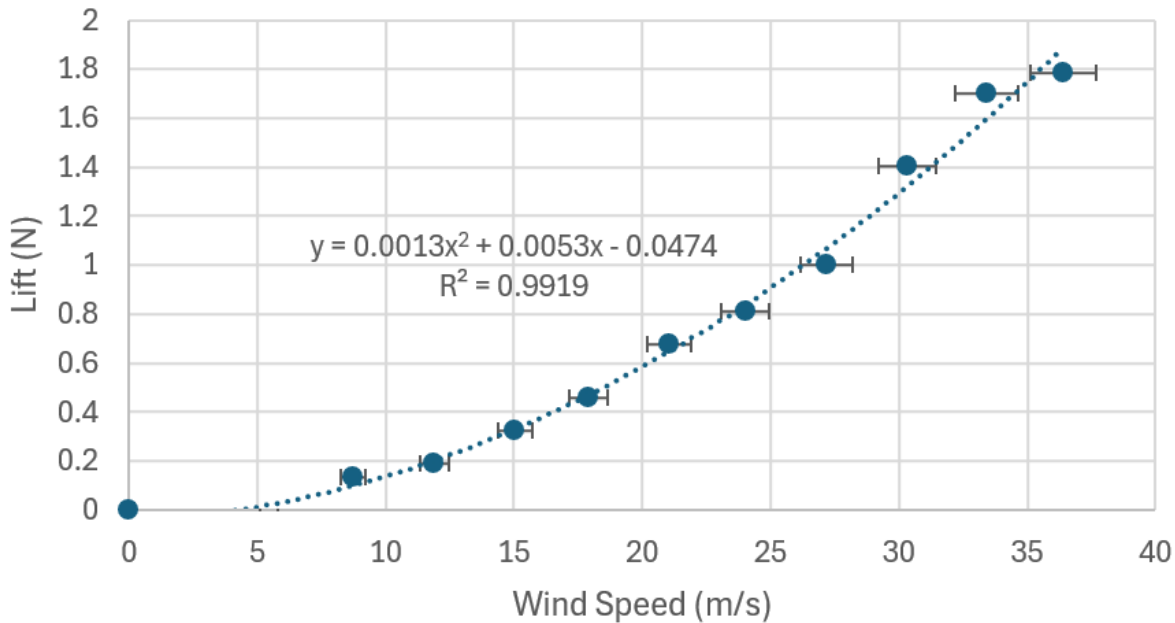


Figure 19. Lift vs Wind Speed for zero-degree angle of attack with error bars.

This plot clearly has a parabolic relationship which agrees with equation 7. Equation 7 directly shows that the relationship between the force of lift and the velocity of the fluid is parabolic. The R^2 value is extremely close to 1 which indicates that this curve best fits the data well. In a later section of the report, this graph will be compared with a theoretical lift vs wind speed plot for the NACA 2418 airfoil. This is the main goal of the experiment for our client's needs. From the force of lift and the calibration data, the coefficient of lift can be calculated using Equation 8. The following figure represents the coefficient of lift calculated for each wind speed. The remaining coefficient of lift vs wind speed plots for the other trials can be found in Appendix V.

Coefficient of Lift VS Wind Speed

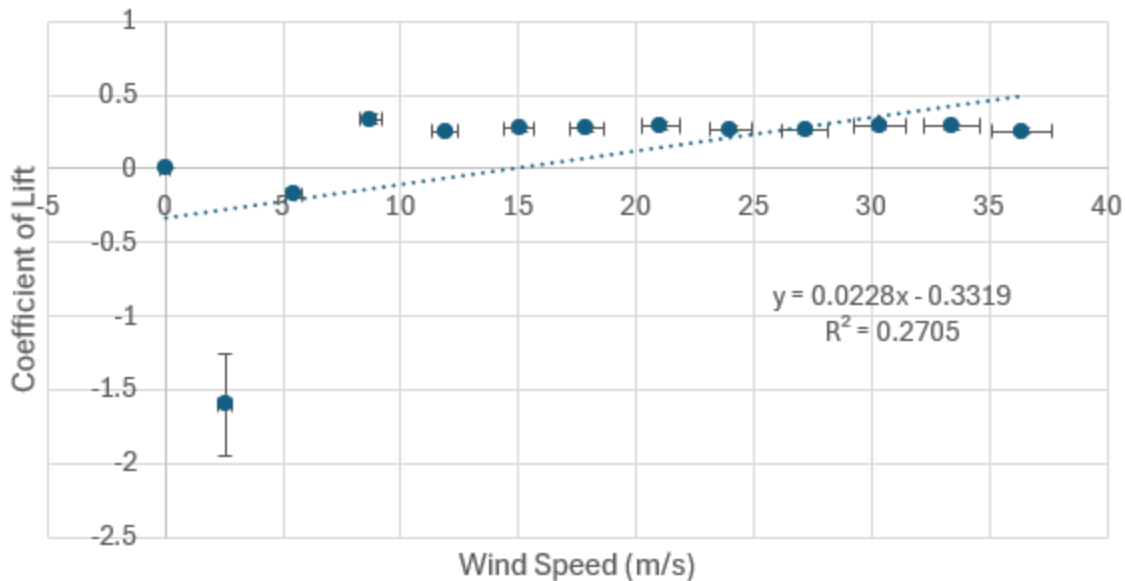


Figure 20. Coefficient of Lift vs Wind Speed for zero-degree angle of attack with error bars and outliers included.

In the above chart, the error bars for coefficient of lift are not visible because of the lower error values calculated using error propagation. Since the coefficient of lift is a constant characteristic for airfoils, it is expected that the coefficient of lift is largely unaffected by changing the wind speed. *Figure 20* demonstrates this because of how close the values are regardless of increasing speed. However, at low speeds, it is difficult to measure the coefficient of lift resulting in negative values and outliers. This is likely due to the accuracy of the experimental rig itself in collecting the pressure data at low speeds. This is also likely to be due to human error in the inability to read small pressure difference using manometers accurately. In the next figure, the first three outlying data points are omitted, and the coefficient of lift could be more easily approximated.

Coefficient of Lift VS Wind Speed (Outliers Removed)

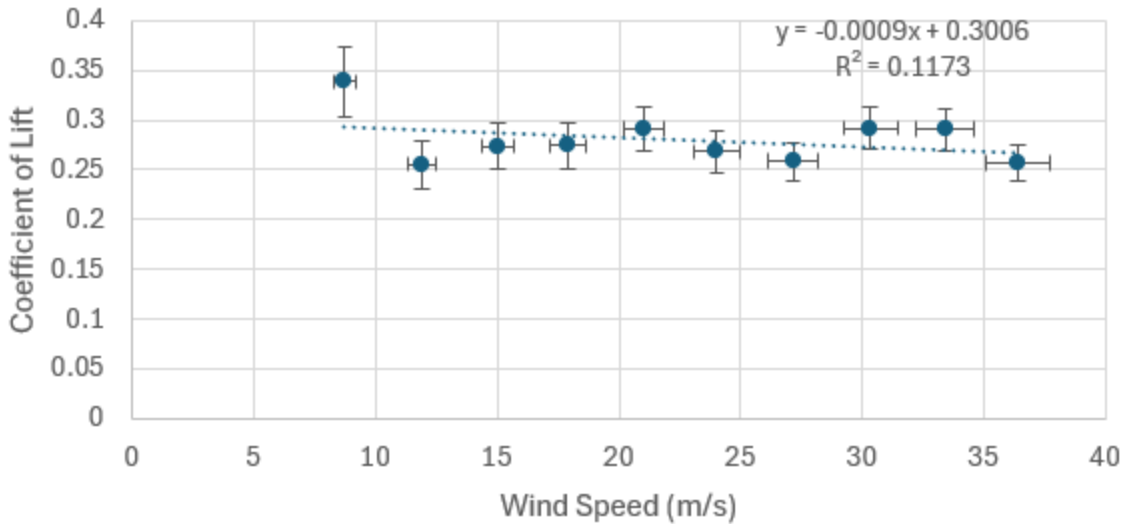


Figure 21. Coefficient of Lift vs Wind Speed for zero-degree angle of attack with error bars and outliers omitted.

Figure 21 demonstrates how the coefficient of lift varies between 0.25 and 0.35 and thus it can be approximated that the coefficient of lift for the NACA 2418 airfoil at an angle of attack of 0 degrees is about 0.3.

Varying Angle of Attack

This experiment also explored the effect that angle of attack had on the coefficient of lift and the lift produced by the airfoil. The angle of attack was measured using the digital inclinometer and was changed twice. The first change was to 4.85 degrees and the final angle attack was 3.90 degrees. As seen in *Figure 22*, changing the angle of attack changes the coefficient of lift and the force of lift.

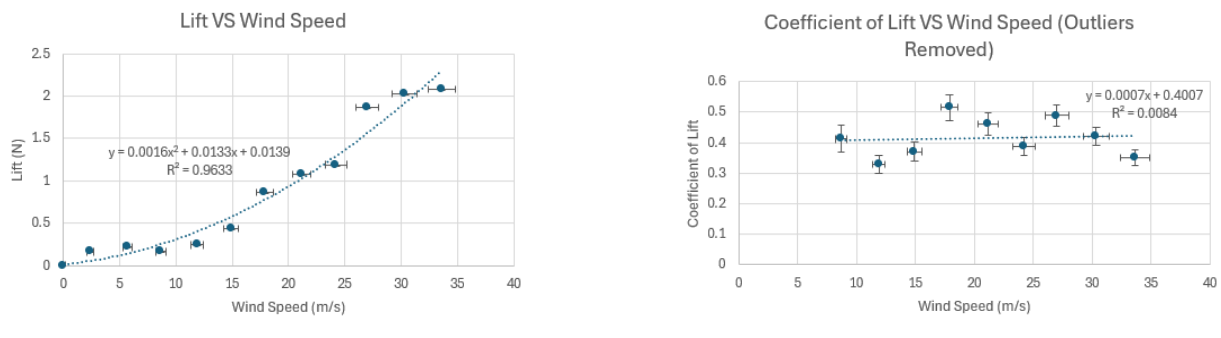


Figure 22. (a) Lift vs Wind Speed and (b) Coefficient of Lift vs Wind Speed (outliers removed) at an angle of attack of 4.85°

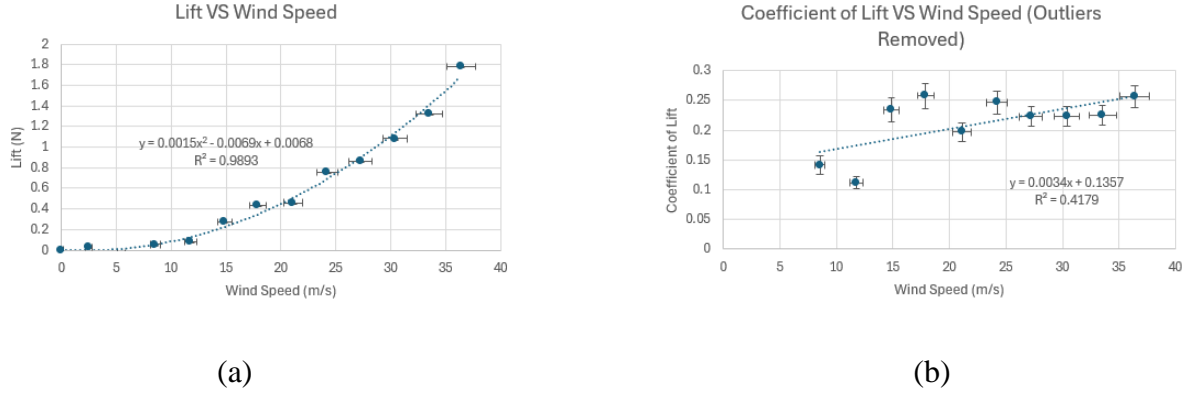


Figure 23. (a) Lift vs Wind Speed and (b) Coefficient of Lift vs Wind Speed (outliers removed) at an angle of attack of 3.90°

As the angle of attack increased, the maximum lift also increased. This makes sense since increasing the angle of attack should increase lift until the critical angle of attack and then decrease after, but there is a point where if the angle of attack is too high, there will be stall. As the angle of attack increases the coefficient of lift also increases. Between trials 2 and 3, increasing the angle of attack also caused a greater spread in the data. While in trial 1, the range of coefficient values was between 0.25 and 0.35, the range in trial 2 is 0.35 and 0.55, and the range in trial 3 is 0.1 and 0.3. It is likely that this uncertainty is also related to the design of the experimental rig because of how the initial design was created with only a zero-degree angle of attack in mind.

Flaws in Data Collection

One flaw that was realized within the experimental rig was that the placement of the hypodermic needles inside the airfoils was important for correctly conducting the force, lift, and coefficient of lift calculations. To make sure that the forces acting on top of the airfoil are subtracted from the forces acting on the bottom, students must make sure that forces A-C correlate to the top of the airfoil and forces D-F correlate to the bottom of the airfoil. For the third trial, the order of the needles inside the airfoil was not correct and thus the data for the third trial had to be adjusted. These incorrect plots that were generated for trial 3 can be found *Appendix VA*. The data for this trial was adjusted by ordering the pressure data from greatest to smallest for pressures A-F since this trend was observed in trials 1 and 2. By looking at these plots, none of the correlations observed in trials 1 and 2 can be found.

The manometers were set up so that one end was always to atmospheric pressure. This resulted in one main problem, a pressure spike that sucked out all the water when the angle of attack and air speed were too high. This pressure spike took place on the pressure tap labeled as "A" which corresponds with the top pressure tap near the leading edge of the airfoil. The pressure spike occurring at this specific location makes sense since this is the point where we expect there to be the greatest pressure difference. As a result of this issue, the data points for the 60hz speed at the 4.85-degree angle of attack trial failed since turning the knob to 60 Hz caused the water to get sucked out of the manometer. This is interesting since data was easily collected at 55 Hz but

once 60 Hz was achieved, the data collection was no longer viable. This issue was fixed for subsequent trials by draining the water back into the manometer and lowering the angle of attack.

A solution to the pressure spike issue was provided by the advisors for this project, Professor Kamau Wright and Professor David Wooton. They suggested that instead of having the ends of the manometer open to the atmospheric pressure, the ends should be connected to the dynamic pressure inside the wind tunnel. This would ensure that the manometers are measuring the difference between the dynamic pressure in the wind tunnel and the pressure at the pressure taps on the airfoil. Since this difference is less than the difference between the pressure taps and atmospheric, there were no pressure spikes that resulted in the water being sucked out of the manometer even though the wind tunnel was set to 60 Hz and the airfoil had a 10-degree angle of attack.

Two more trials were conducted after connecting the free end of each manometer to tubing that led into the wind tunnel. While the goal of this was to mitigate pressure spikes, these trials were conducted to compare against the first 3 trials to see how much of an impact the pressure inside the wind tunnel has on the data. For the fourth trial, the angle of attack was set to 0 degrees so it could be directly compared to trial 1 data. As seen in the plots in *Appendix VE*, the pressure and force plots have similar trends between trials 1 and 4. Both sets of data are polynomial as proven by the R-squared values. Furthermore, the lift graphs that were generated were also within similar ranges for trials 1 and 4. The discrepancy between the two sets of data is present in the graphs for the coefficient of lift with and without the outliers removed.

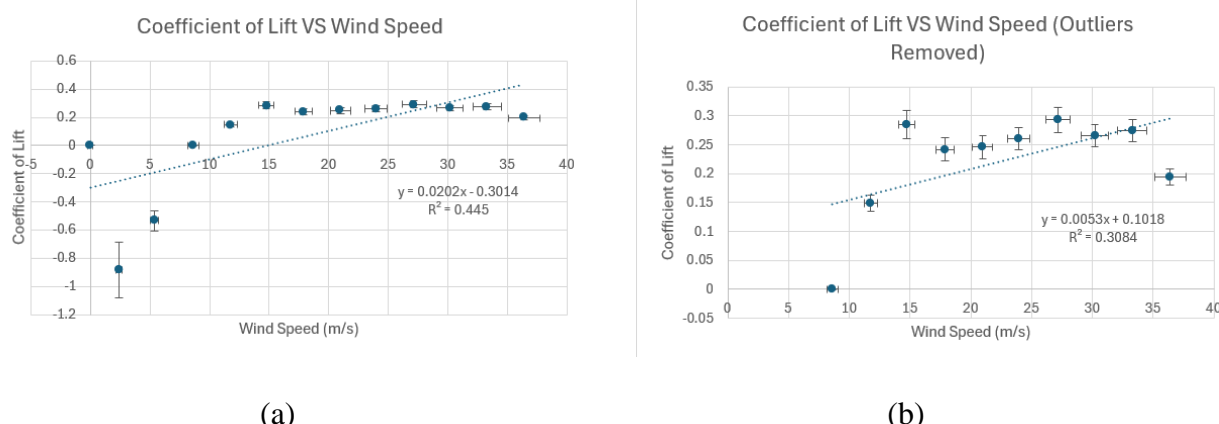


Figure 24. Coefficient of Lift vs Wind Speed for zero-degree angle of attack with error bars and (a) with and (b) without outliers when the pressure inside the wind tunnel was used.

Compared to *Figure 20* and *Figure 21*, *Figure 24* has more outlying values and a greater spread of data. Thus, data from trial 4 makes it difficult to approximate an appropriate coefficient of lift due to the lower precision of the data collected. It is possible that this is due to possible leaks in the tubing that leads into the wind tunnel. This tubing existed prior to this experiment and fittings that were connected to the tubing showed signs of deterioration over time.

Now that the pressure spikes were mitigated, a much higher angle of attack could be explored. Originally, minimal tests with around a 10-degree angle of attack resulted in large pressure

spikes, but the final trial, trial 5, was conducted at a 10-degree angle of attack with no issues. Similar trends to the first three trials followed here as well because compared to trial 4, the lift and coefficient of lift were higher due to the greater angle of attack. Also, like trial 4, the spread of the data was still larger than the spread in the first three trials, further portraying the shortcomings of the experimental rig. The trial 5 plots relating pressure and wind speed, forces, and wind speed, lift and wind speed, and coefficient of lift and wind speed can be found in *Appendix V*.

Experimental vs Theoretical

The NACA 2418 is a well-studied airfoil and there exists data relating the coefficient of lift to the angle of attack. In the figure shown below, this relationship is shown and can be used to compare the experimental coefficients of lift found through the wind tunnel test to accepted values of coefficients of lift.

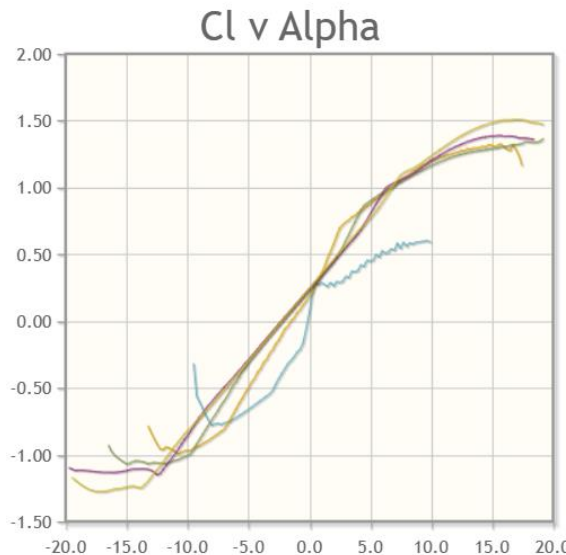


Figure 25. NACA 2418 Coefficient of Lift vs angle of attack graph from airfoiltools.com.

As seen in *Figure 25*, the coefficient of lift for a 0-degree angle of attack is about 0.25. This correlates well with both trials 1 and 4 where data was collected for 0-degree angle of attack. As seen in *Figure 21* and *Figure 24*, the coefficient of lift was approximated to be between 0.3 and 0.25. The discrepancy could be attributed to inconsistencies in the airfoil shape due to damage from handling the resin-printed airfoil or pressure leakage in the system. Regardless, the theoretical and experimental values compare well against each other. However, figure 25 also demonstrates that at an angle of attack of 5 degrees and 10 degrees, the coefficient of lift is about 0.8 and 1.2, respectively. By looking at figure 22 and figure 65 from *Appendix V*, the experimental coefficient of lift for the angles of attacks listed previously are much lower and closer to the coefficient of lift for 0-degrees angle of attack. Thus, this demonstrates how the experimental rig is inefficient in characterizing coefficient of lift for different angles of attack but is fairly accurate for 0-degree angle of attack.

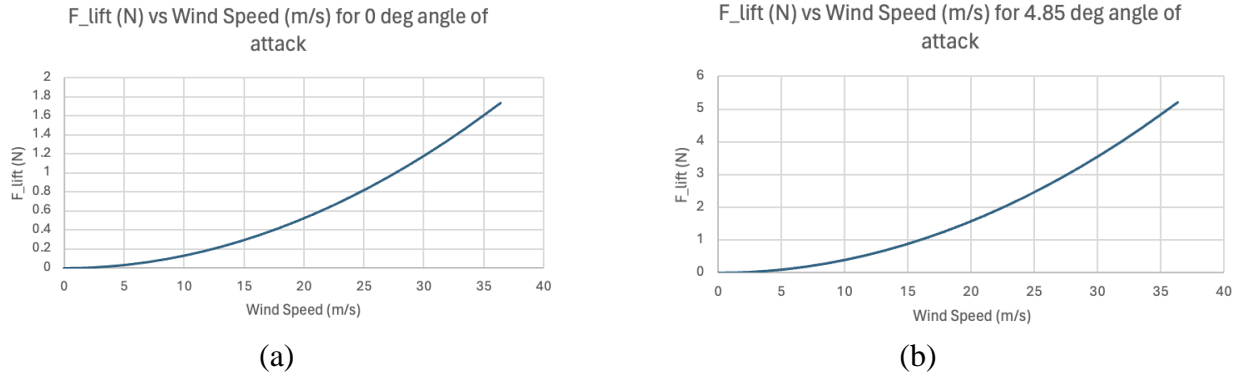


Figure 26. Theoretical plots relating lift and wind speed for the experimental angles of attack, (a) 0° and (b) 4.85° , that were used in the experimental trials.

In *Figure 26*, theoretical curves were generated for the experimental angle of attacks tested in trials 1 and 2 using the NACA 2418 coefficient of lift vs angle of attack graph in *Figure 25*. While the plot in *Figure 26 (a)* correlates very well with the experimental graph in *Figure 19*, the plot *Figure 26 (b)* shows that the lift for a 5-degree angle of attack should have been magnitudes higher when compared to *Figure 22*. This theoretical chart specifically demonstrates the inaccuracy related to determining the lift for angles of attack greater than 0. One more theoretical chart for 10 degrees angle of attack can be found in *Appendix VI*.

Conclusion

Our client's original goal was to have an experimental rig for students in the fluid mechanics and aerodynamics classes to gain experience with aerospace theory and equipment. This experiment has students make use of the wind tunnel, which is a key piece of aerodynamic equipment. Students have to manually take data which allows them to gain a greater understanding of the process and work more closely with the equipment. They would make use of aerodynamic theory by using the formulas in this report to calculate lift and coefficient of lift. Students can explore the effect angle of attack has on these values and potentially, they could perform the experiment in a way to determine the critical angle of attack. They could also calculate the stall angle.

This experiment proved that lift and lift coefficient can be successfully calculated by using manometers and pressure taps on a 3D printed airfoil. Not only, was the data collected, the data was also accurate for the zero-degree angle of attack. It compares very well to the theoretical plot which allows us to validate our data, the entire experimental rig, and the experiment itself. The lift data collected had a parabolic trend, which agrees with the equations that govern the relationships. At higher speeds, the lift coefficients calculated were almost constant. At lower air speeds, this was not the case. This also supports the fact that the optimal range of frequencies for the experimental rig is 10 Hz to 60 Hz. Data collection and accurate readings are very difficult under the 10 Hz frequency.

This experiment was performed with a NACA 2418 airfoil that was modified so that it could be mounted in the airfoil test section. Since that is a standard airfoil, any airfoil profile can be used as long as it meets the mounting requirements. This would allow students to study the different airfoil profiles and the different results they produce.

Changing the angle of attack increased the coefficient of lift and the force of lift. This follows with conventional theory since this relationship will hold true until the critical angle of attack is reached. As the angle of attack was increased, there were issues in the experimental rig. These issues were addressed by changing the pressure difference measured in the manometers.

There are many future steps for this project. Different airfoil profiles, different materials, more pressure taps, etc. are all examples of physical changes that can be made to the rig to improve the data collected. The experiment itself can be modified so that students can study specific phenomenon. The hope of this project is that it could become a tool for professors to use as labs in classes like fluid mechanics or aerodynamics. Potentially, this could become an M1 lab that students perform in ME360-Experimentation.

Bibliography

- [1] NACA 2418 (NACA2418-IL), <http://airfoiltools.com/airfoil/details?airfoil=naca2418-il> (accessed May 7, 2024).
- [2] “Lift coefficient,” NASA, <https://www1.grc.nasa.gov/beginners-guide-to-aeronautics/lift-coefficient/> (accessed May 7, 2024).
- [3] J. W. Mitchell, R. W. Fox, and A. T. McDonald, *Fox and McDonald’s Introduction to Fluid Mechanics*. Hoboken NJ: John Wiley & Sons, Inc., 2020.

Appendix I: Problem Formulation Diagram

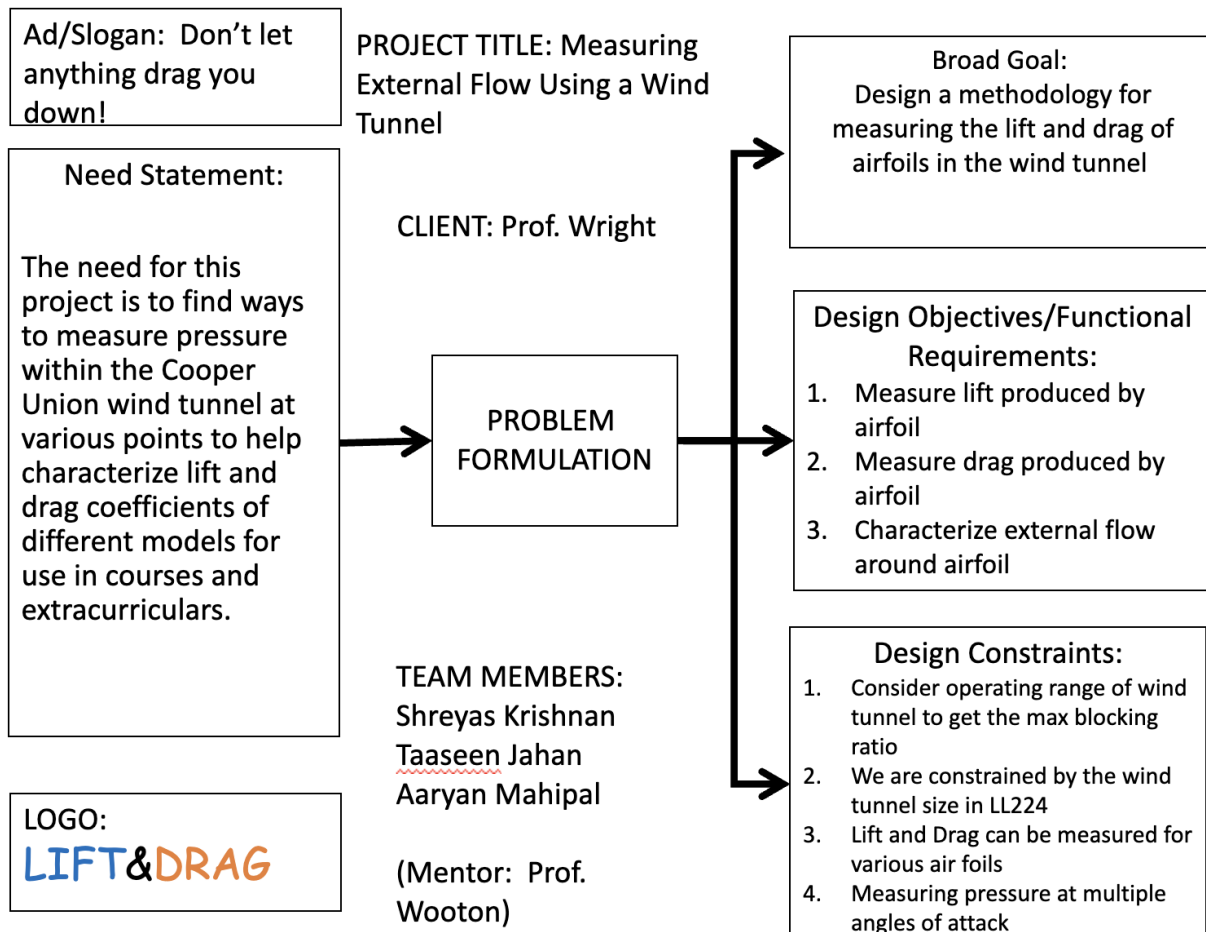


Figure 27. Problem Formulation Diagram developed towards the beginning of the project

Appendix II: BOM

Table 2. Bill of Materials

Item	Company	Description	Brand	Part #	Price	Quantity	Comment
0-3KPa Pressure Gauge Manometer	Amazon	Conventional Manometer for Pressure Data Collection	Totority	B09KLF PFHW	\$17.49	6	For the airfoil rig
Clear PVC Vinyl Tubing (0.25" OD)	Amazon	Flexible Tubing to connect manometer to airfoil.	EZ-FLO	B07Q1D 14HF	\$5.98	2	To connect manometers to airfoil
Clear PVC Vinyl Tubing (0.15" OD)	Amazon	Flexible Tubing to connect manometer to airfoil	uxcell	a191213 00ux008 6	\$5.99	2	To connect manometers to airfoil
Clear PVC Vinyl Tubing (0.39" OD)	Amazon	Flexible Tubing to connect manometer to airfoil	uxcell	a191213 00ux009 8	\$9.59	2	To connect manometers to airfoil
Wintact Digital Anemometer	Amazon	Wintact Digital Anemometer for calibrating wind tunnel.	Wintact	B08345 KBNP	\$29.99	1	For wind tunnel calibration
HTI Digital Anemometer	AliExpress	HTI Digital Anemometer for calibrating the wind tunnel	HTI	AO-HT-81	\$28.79	1	For wind tunnel calibration
24" x 26" White Acrylic Sheet	Canal Plastics	Acrylic Mount to mount all the manometers	Canal Plastics	N/A	\$36.00	1	To mount manometers
White PLA	Amazon	PLA needed for 3D printing various parts	ELEGOO	B0BM74 46JH	\$14.99	1	Print anything we need
Hose Clamps	Amazon	Hose clamps to secure tubing to manometers	Steelsoft	B0C4V6 BCPH	\$7.99	1	Seal tubing together
Mounting Brackets	Amazon	Mounting brackets to mount manometers	MONKIP-AER	B0C814 1GB1	\$6.55	1	To mount manometers onto acrylic
Hypodermic Tubing (1 ft)	MicroGroup	Maximum OD 0.0625"	N/A	304H16.5	\$7.08	10	To interface with the pressure tap holes on airfoil
Standoffs	Amazon	Standoffs to mount setup	Osrings	B0C814 1GB1	\$11.99	1	To mount rig on wind tunnel wall
Inclinometer	Amazon	Used to set airfoil at certain angle of attack	GemRed	82413	\$43.99	1	Measures Angle of Attack
3/8" NPT Hex Nut	Amazon	Used to constrain pipe against test section door	DERNORD	B0BFB5 F9D8	\$8.99	1	Constrains pipe and airfoil against plexiglass door
3/8" NPT Hex Cap	Ace Hardware	Used to mount pipe against airfoil	Bilco	7532880 00230	\$3.59	1	Mounts airfoil and shields pressure tubing
3/8" NPT Nipple, 5" Length	Ace Hardware	Routes tubes and mounts airfoil	STZ Industries	309UP38 X5	\$6.59	1	Mounts airfoil and shields pressure tubing

Link: https://cooperunion.sharepoint.com/:x/s/Section_ME-360-B-2024SP-ExternalFlow-AirfoilandWindTunnel/EeXqY84HCUBPrzMwr11ME68B8po9sc0m4hpaG-cGqUBs7A?e=Sr7iIm

The first item on the list is the manometers. The goal was to maintain a low cost, so small manometers were chosen. Professor Wooton provided a link to a larger size manometer that was within budget. These manometers were perfect since they are easy to mount, and they have a built-in ruler to measure the height of the liquid. Six manometers are needed since there are six separate pressure taps on the airfoil.

Tubing was needed to connect the hypodermic needles to the manometers themselves. This tubing has a tight enough diameter, and two spools were needed since the distance between the manometers and the actual airfoil is relatively large.

A new anemometer was needed since the current one that belongs to the ME Department is not rated for the highest air speeds that the wind tunnel produces. Even though it produced data, we cannot guarantee accuracy. Both the ME Department anemometer and the new anemometer have the same instrumental error and uncertainty.

The large acrylic sheet was needed to mount the manometers in a neat and organized way and so those manometers can be mounted on the wind tunnel room wall. The PLA was not purchased but was included as part of the BOM since it was used to 3D print various parts, such as the air foil mount. The hose clamps were needed to ensure that the tubing was adequately connected to the manometers and that were no air leaks. The L-brackets were needed to mount the six manometers to the acrylic sheet. The hypodermic needles were needed to interface with the pressure tap ports on the side of the air foil. Finally, the stand offs were needed to effectively mount the whole system on the walls of the wind tunnel room.

Appendix III: Design Drawings

Initial Prototype

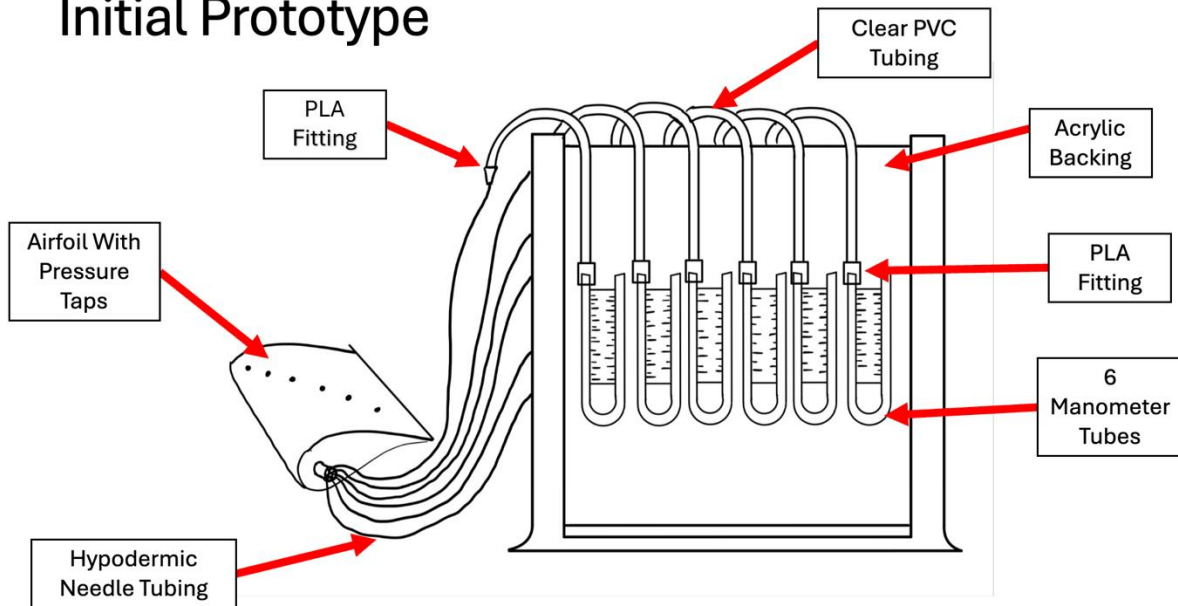


Figure 28. Initial prototype idea drawing

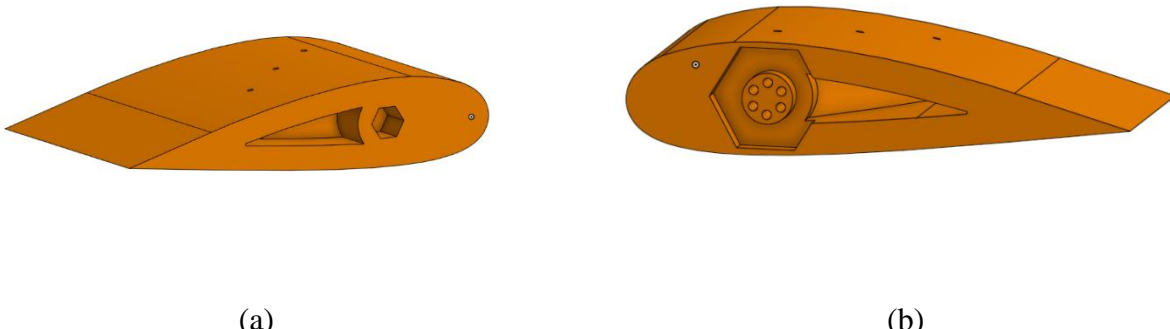


Figure 29. CAD of NACA 2418 Airfoil (a) back view with a port for resin printed hex shaft and (b) front view with port for NPT threaded hex cap and channels for hypodermic needles.



Figure 30. CAD of hex shaft used to mount the airfoil to the rear end of the wind tunnel test section window using a 1/4-20 screw

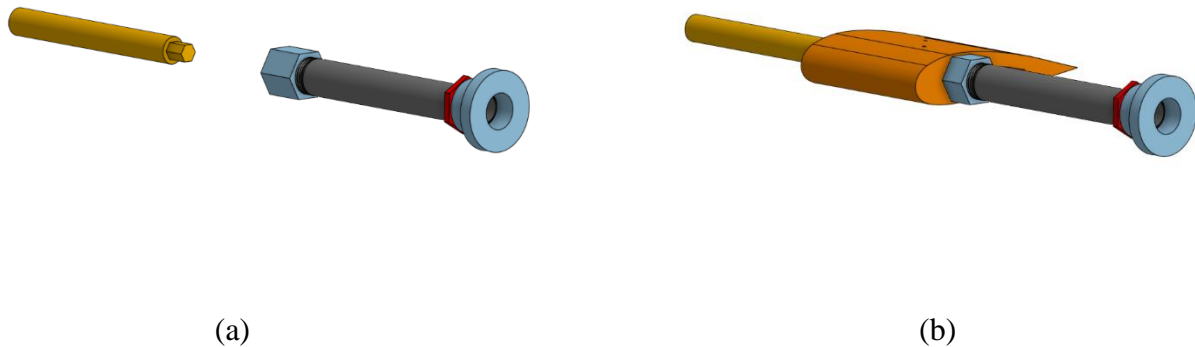


Figure 31. CAD of second airfoil mount prototype (a) without the airfoil attached and (b) with the airfoil attached

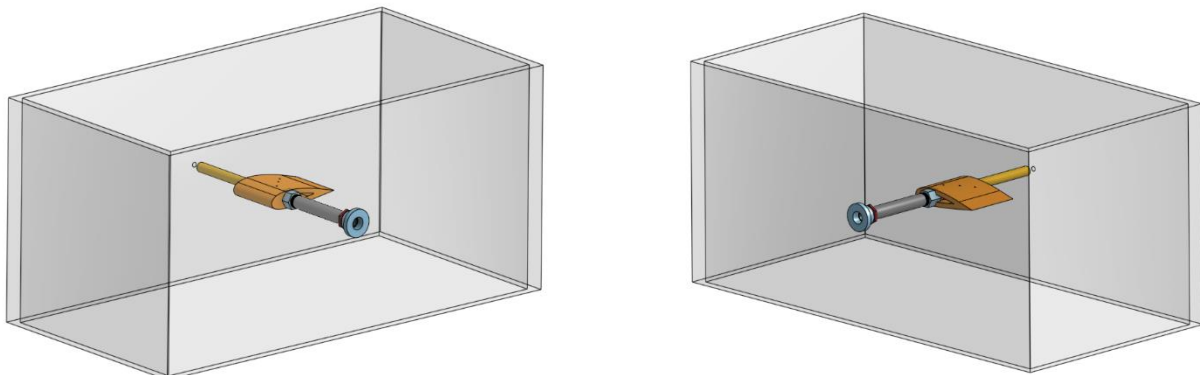


Figure 32. CAD of second airfoil mount prototype with the airfoil attached inside the wind tunnel test section

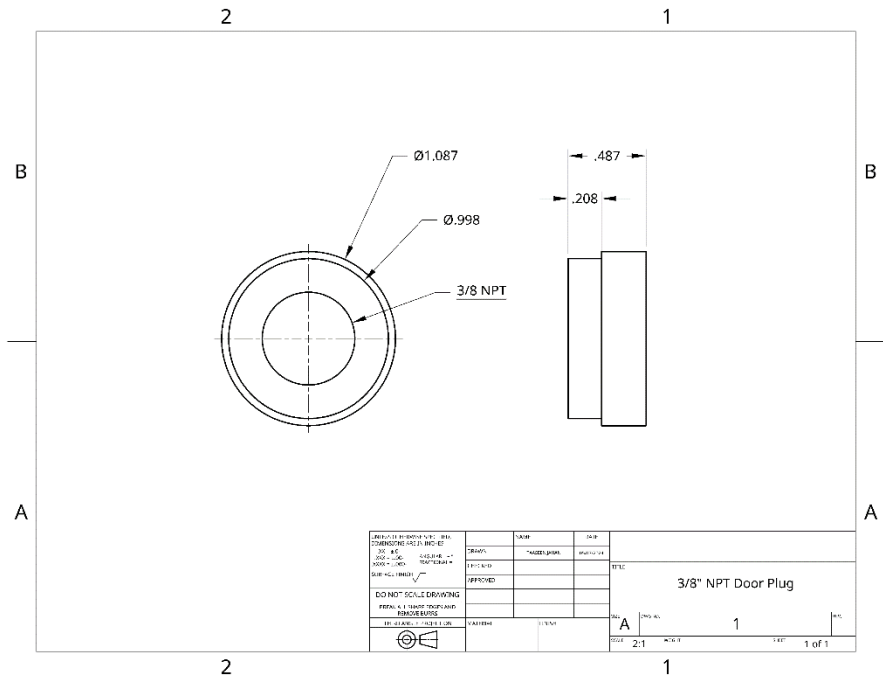


Figure 33. 2D CAD drawing of 3/8" NPT plug that was machined to fit into test section door and constraint 3/8" NPT pipe nipple.

Appendix IV: Wind Tunnel Calibration Data

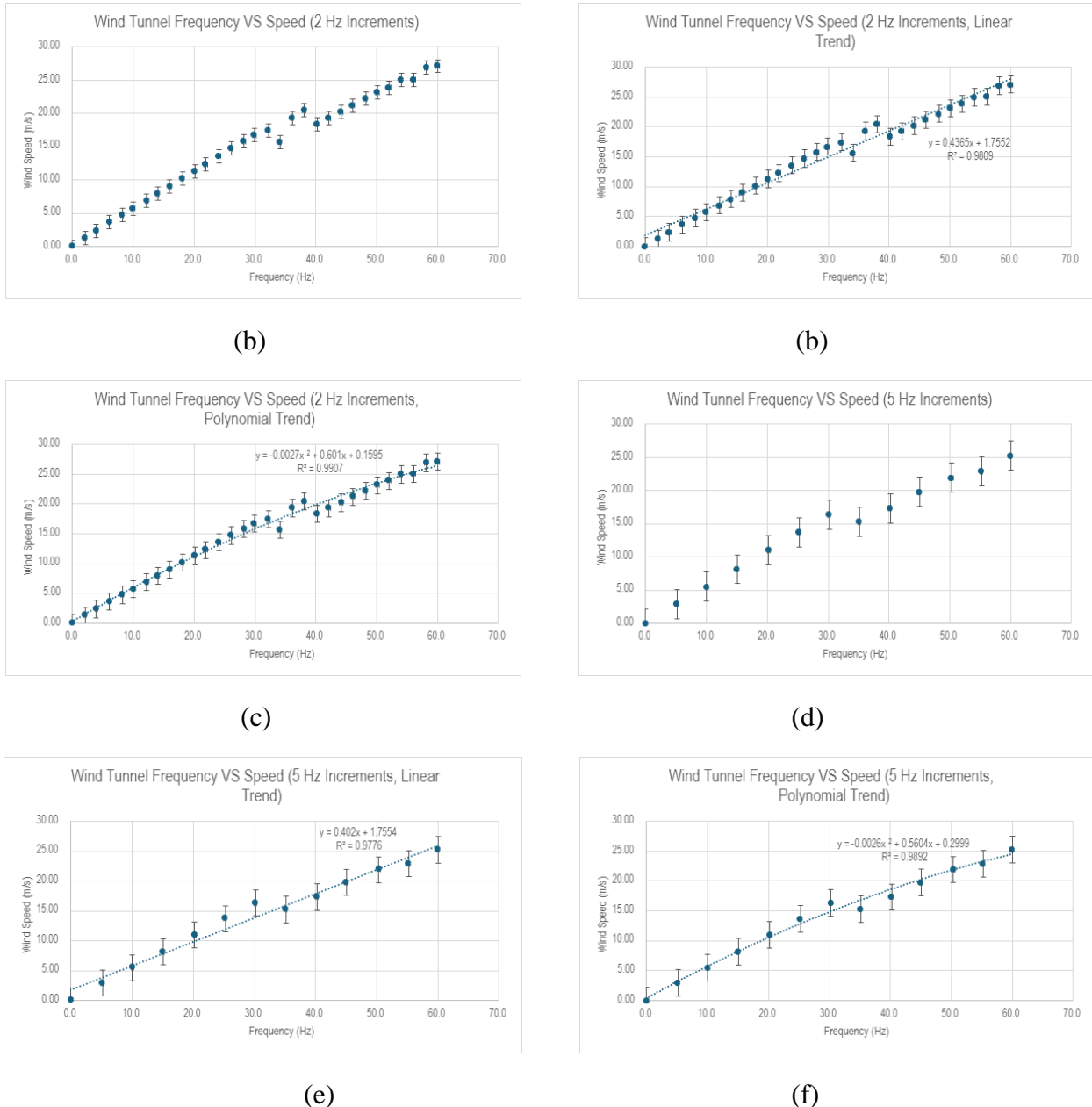
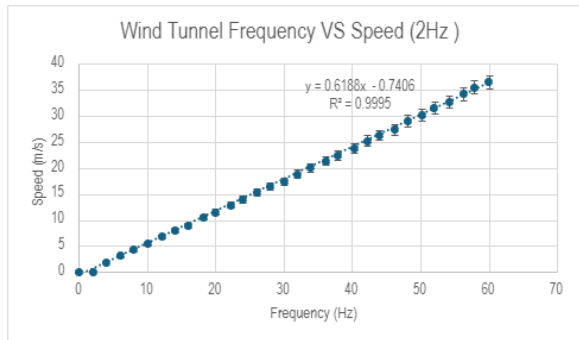
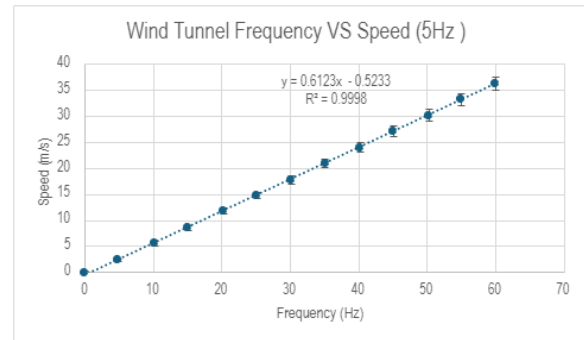


Figure 34. Wind Tunnel frequency vs Speed using HTI Digital Anemometer with 2 Hz increments (a, b and c) and 5hz increments (d, e and f), applying both linear and polynomial trends.



(a)



(b)

Figure 35. Wind Tunnel frequency vs Speed using Wintact Digital Anemometer with (a) 2 Hz increments and (b) 5 Hz increments, applying linear trend to both.

Appendix V: Lift Calculation Data

A. Lift Calculation Data for Trial 1 at 0° angle of attack

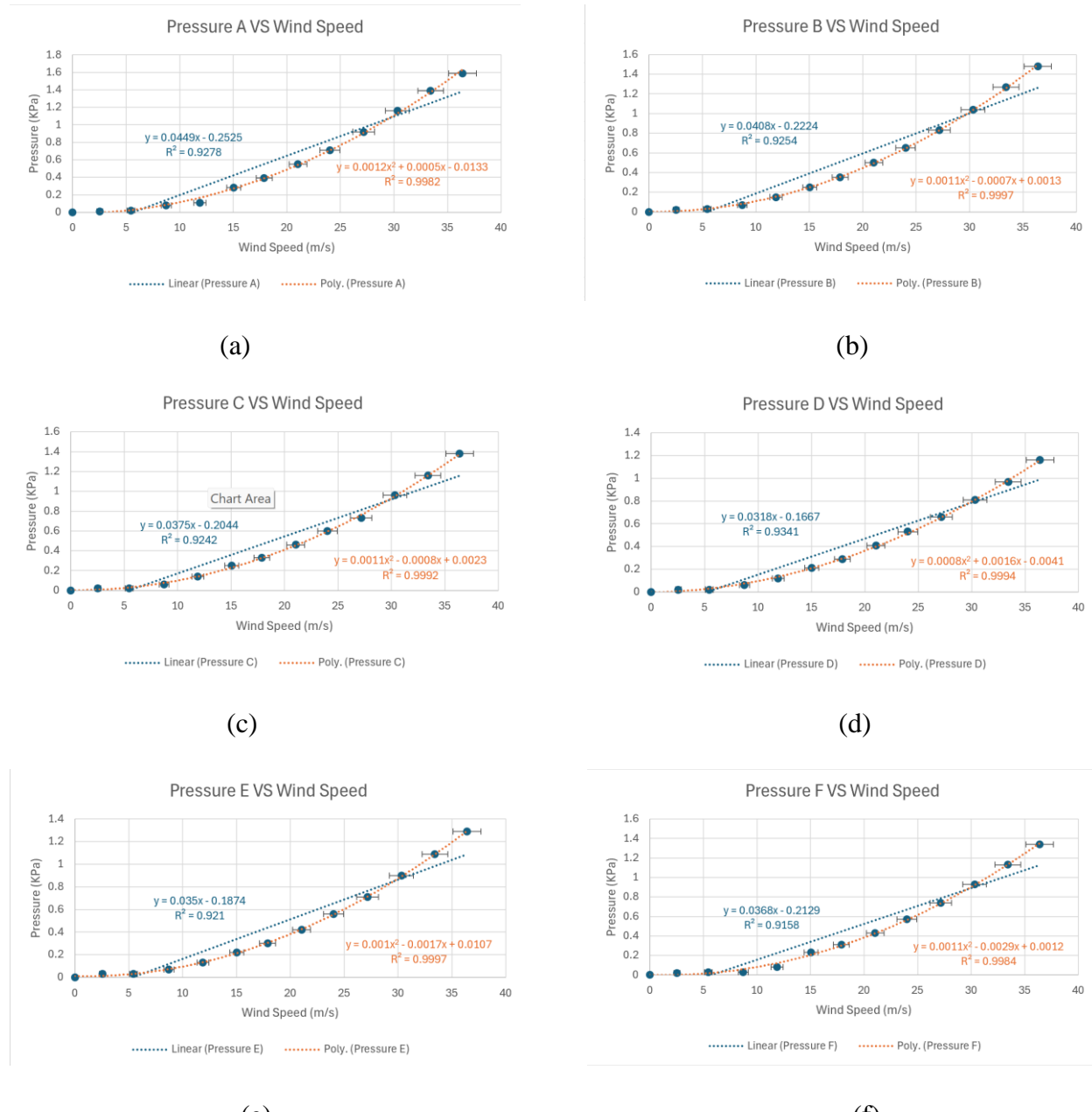


Figure 36. Plots for pressure measurements at varying wind speeds and with linear and polynomial fit for (a) Pressure A vs Wind Speed, (b) Pressure B vs Wind Speed, (c) Pressure C vs Wind Speed, (d) Pressure D vs Wind Speed, (e) Pressure E vs Wind Speed, and (f) Pressure F vs Wind Speed, at an angle of attack of 0°

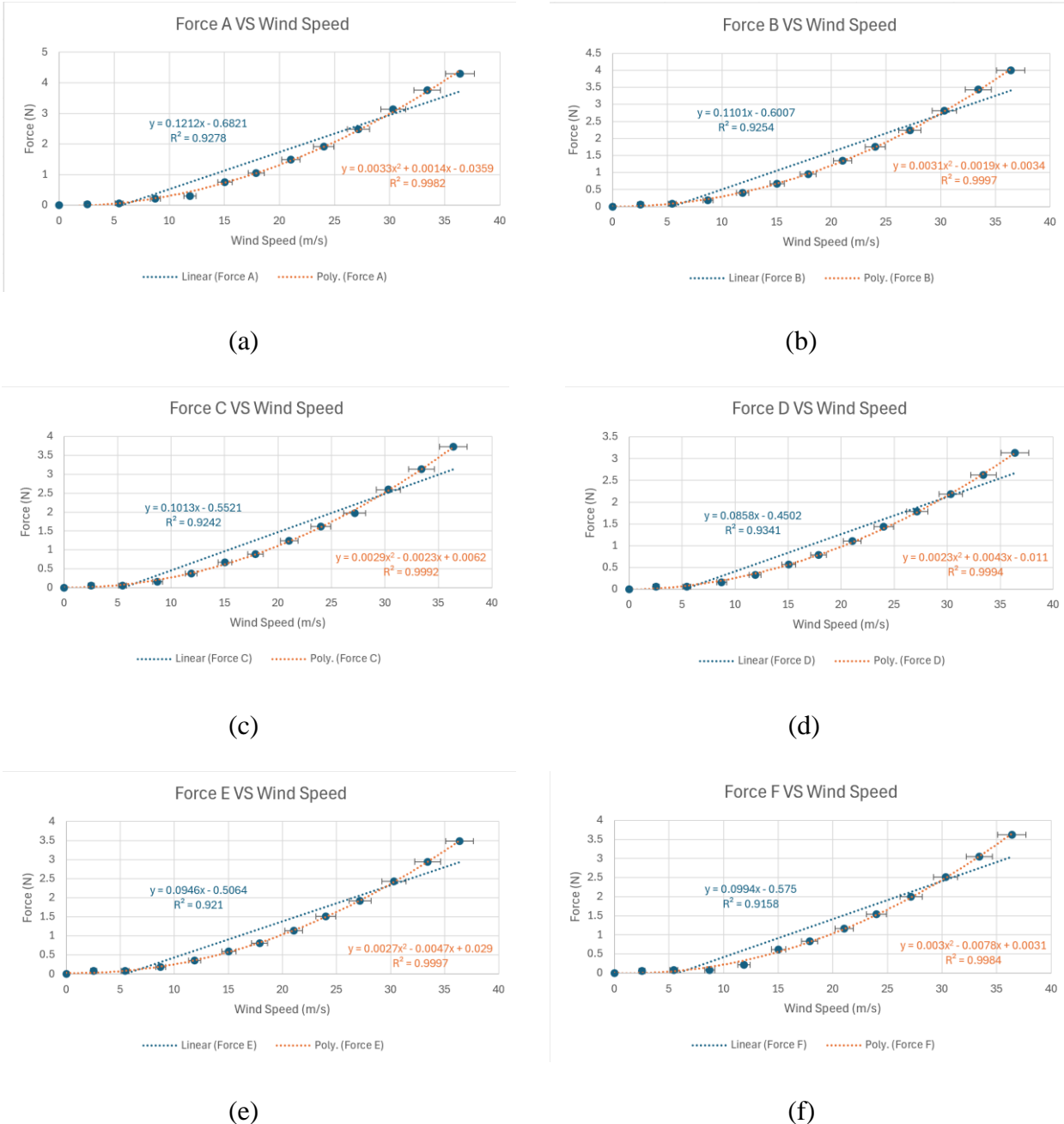


Figure 37. Plots for force measurements at varying wind speeds and with linear and polynomial fit for (a) Force A vs Wind Speed, (b) Force B vs Wind Speed, (c) Force C vs Wind Speed, (d) Force D vs Wind Speed, (e) Force E vs Wind Speed, and (f) Force F vs Wind Speed, at an angle of attack of 0°

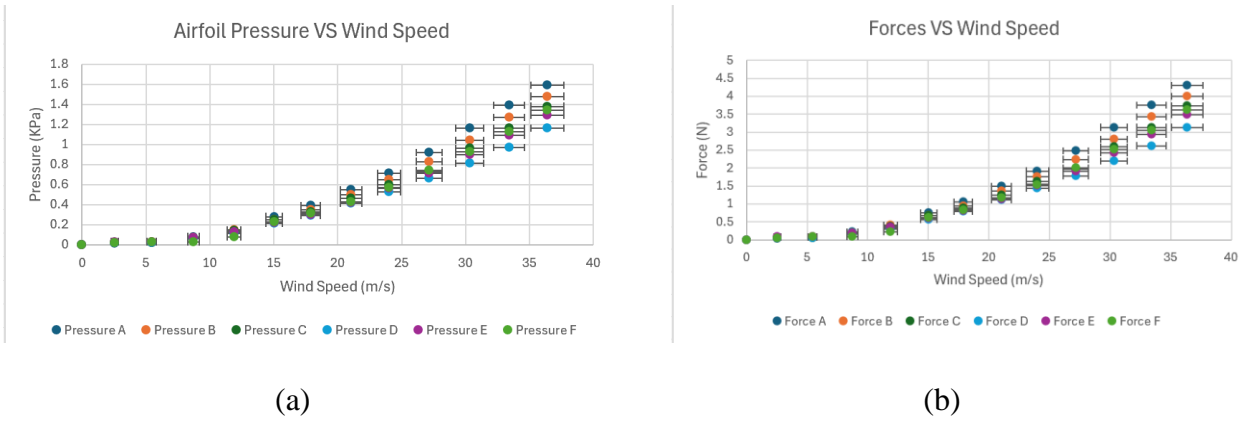


Figure 38. Plots with linear and polynomial fit for (a) Airfoil Pressures vs Wind Speed and (b) Forces vs Wind Speed, at an angle of attack of 0°

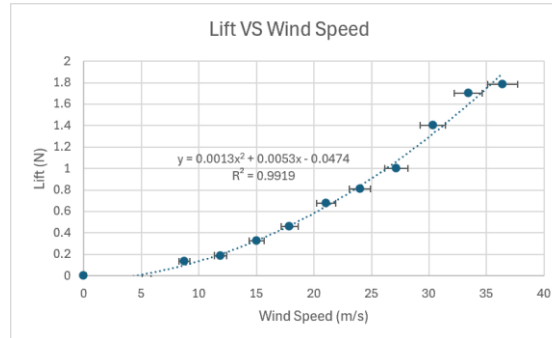


Figure 39. Plot for Lift vs Wind speed with polynomial fit at 0° angle of attack

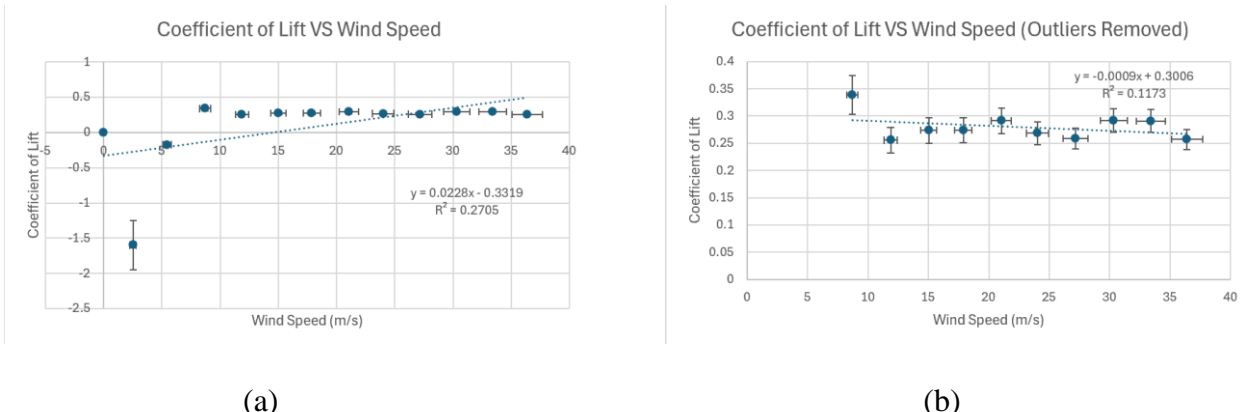


Figure 40. Plot for Coefficient of Lift vs Wind Speed with a polynomial fit at 0° angle of attack
(a) with outliers and (b) without outliers

B. Lift Calculation Data for Trial 2 at 4.85° angle of attack

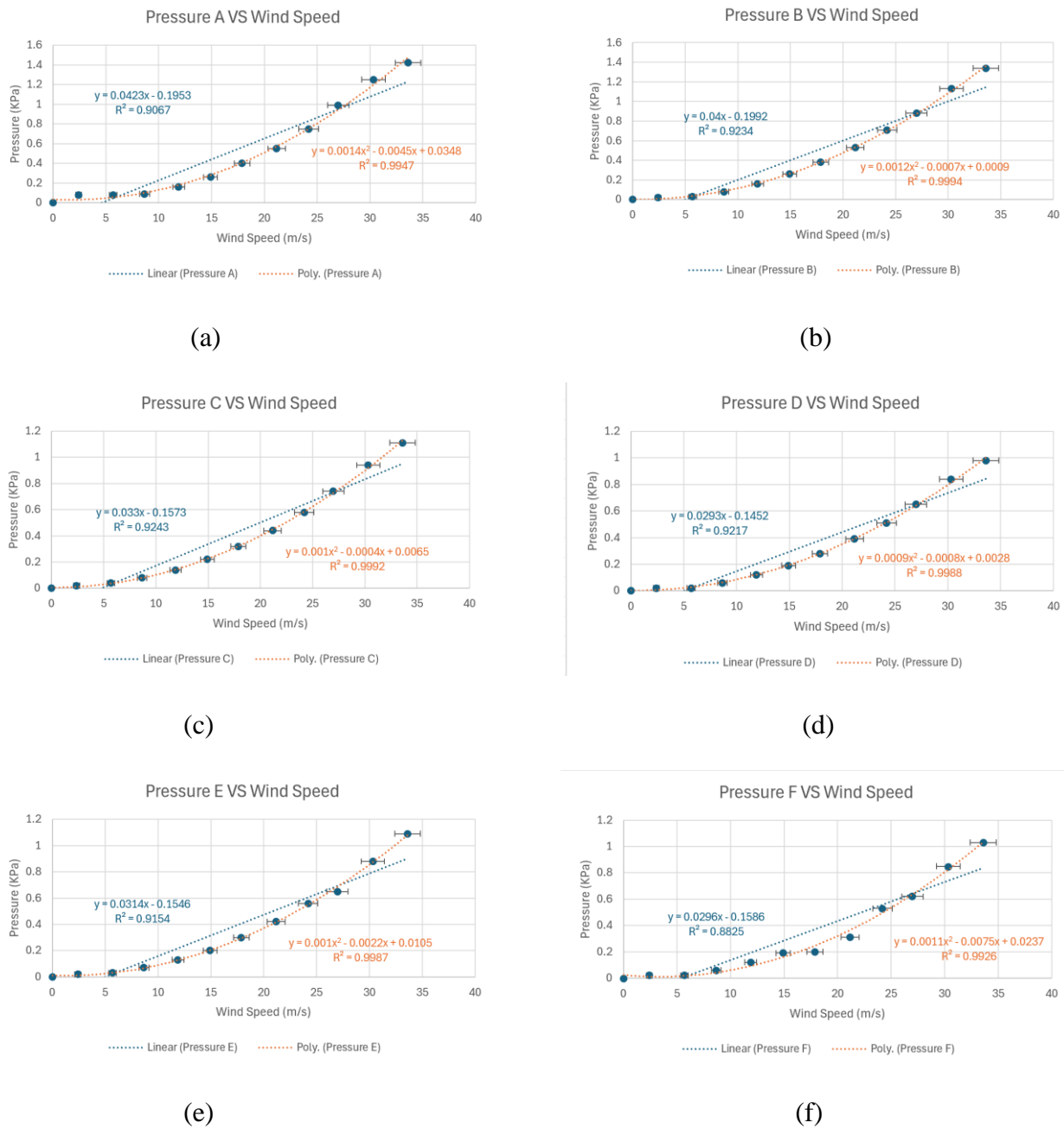


Figure 41. Plots for pressure measurements at varying wind speeds and with linear and polynomial fit for (a) Pressure A vs Wind Speed, (b) Pressure B vs Wind Speed, (c) Pressure C vs Wind Speed, (d) Pressure D vs Wind Speed, (e) Pressure E vs Wind Speed, and (f) Pressure F vs Wind Speed, at an angle of attack of 4.85°

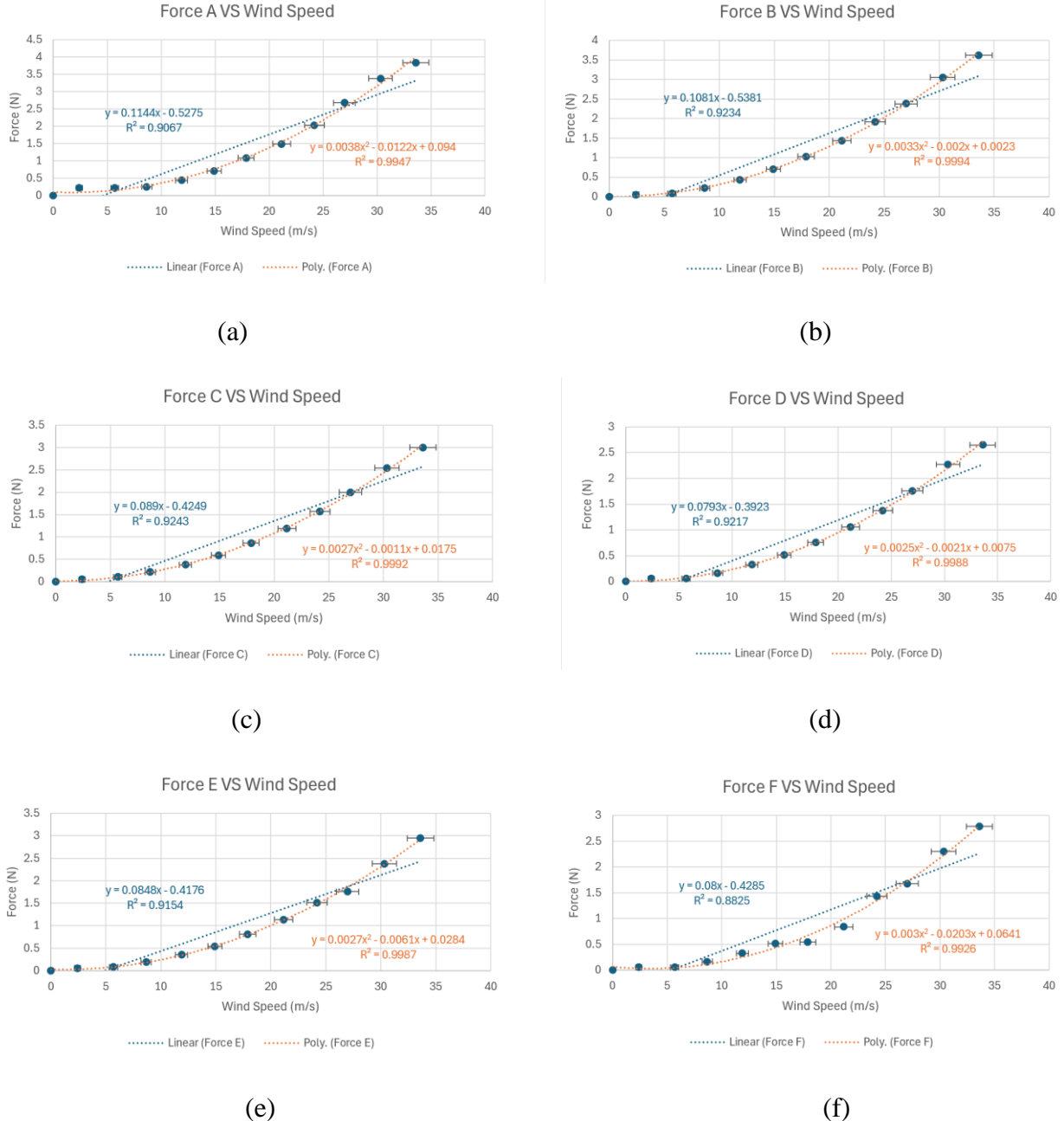


Figure 42. Plots for force measurements at varying wind speeds and with linear and polynomial fit for (a) Force A vs Wind Speed, (b) Force B vs Wind Speed, (c) Force C vs Wind Speed, (d) Force D vs Wind Speed, (e) Force E vs Wind Speed, and (f) Force F vs Wind Speed, at an angle of attack of 4.85°

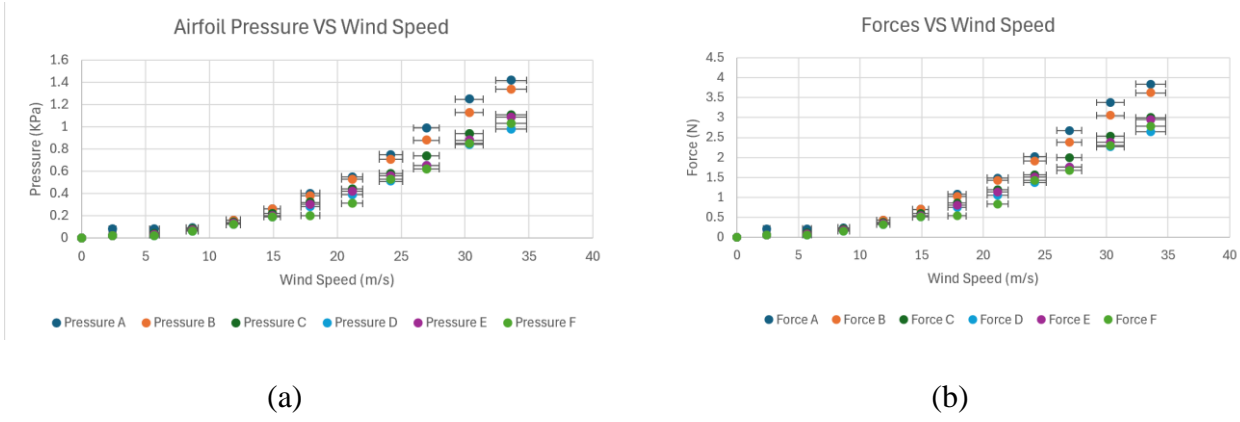


Figure 43. Plots with linear and polynomial fit for (a) Airfoil Pressures vs Wind Speed and (b) Forces vs Wind Speed, at an angle of attack of 4.85°

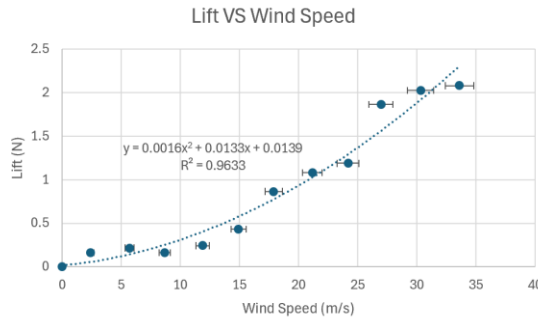


Figure 44. Plot for Lift vs Wind speed with polynomial fit at 4.85° angle of attack

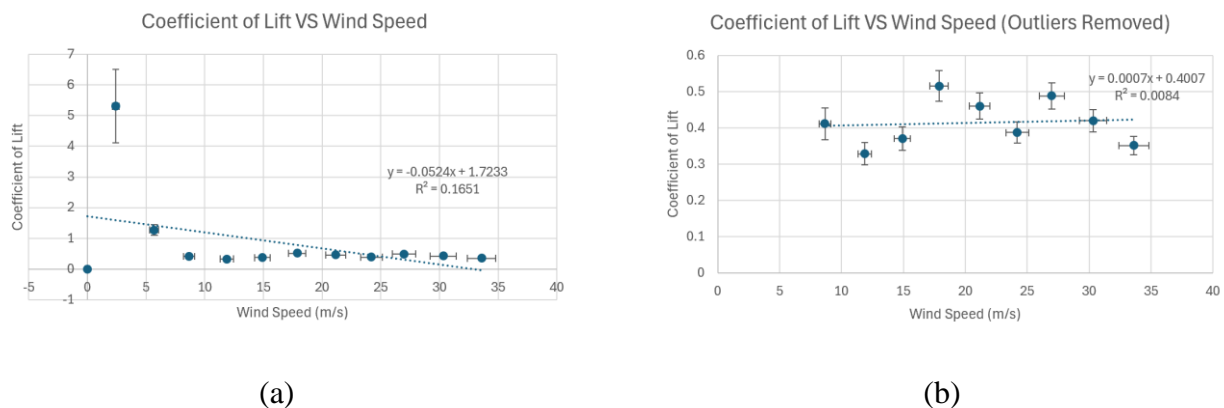


Figure 45. Plot for Coefficient of Lift vs Wind Speed with a polynomial fit at 4.85° angle of attack (a) with outliers and (b) without outliers

C. Corrected Lift Calculation Data for Trial 3 at 3.90° angle of attack

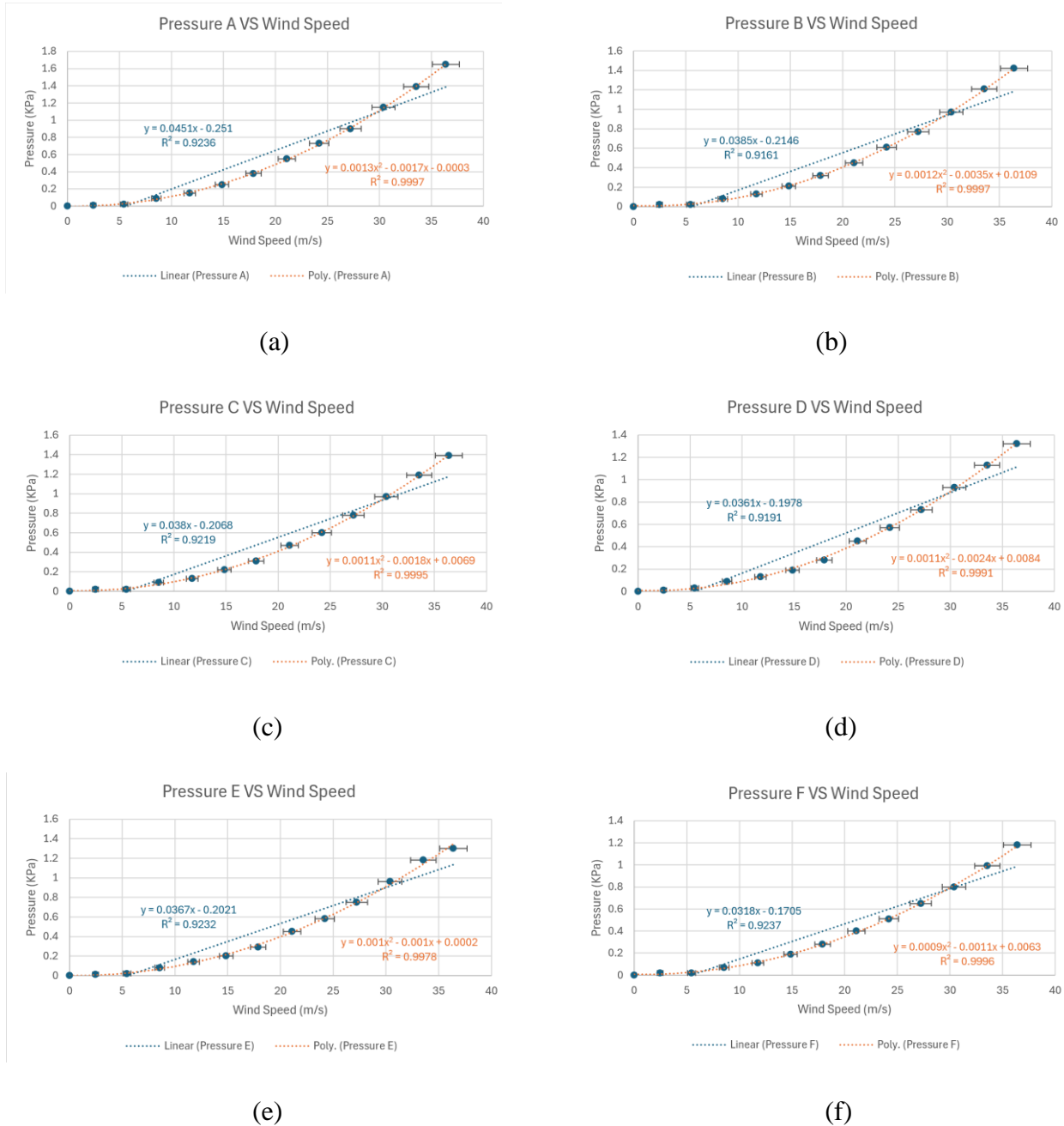


Figure 46. Corrected plots for pressure measurements at varying wind speeds and with linear and polynomial fit for (a) Pressure A vs Wind Speed, (b) Pressure B vs Wind Speed, (c) Pressure C vs Wind Speed, (d) Pressure D vs Wind Speed, (e) Pressure E vs Wind Speed, and (f) Pressure F vs Wind Speed, at an angle of attack of 3.90°

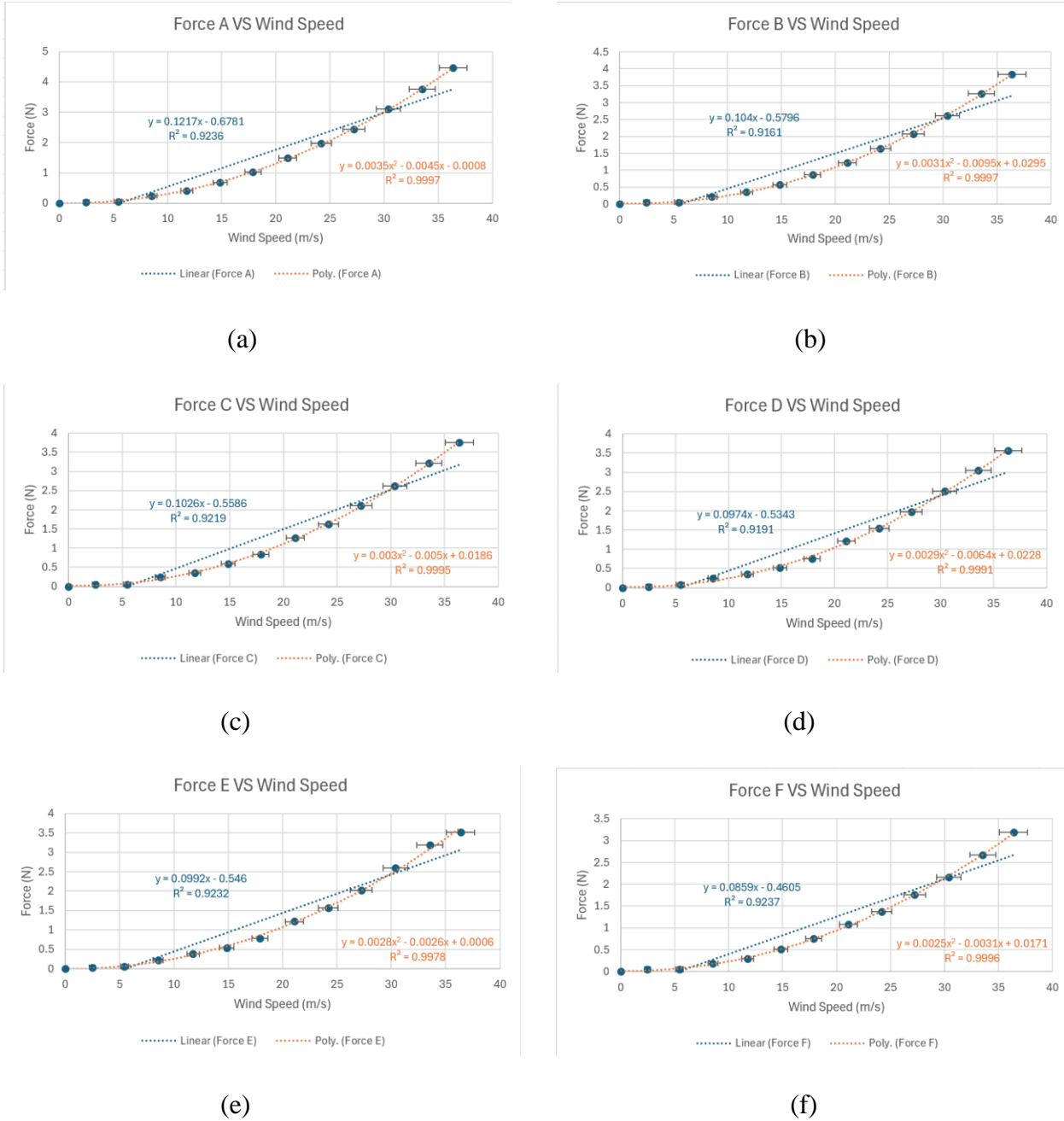


Figure 47. Corrected plots for force measurements at varying wind speeds and with linear and polynomial fit for (a) Force A vs Wind Speed, (b) Force B vs Wind Speed, (c) Force C vs Wind Speed, (d) Force D vs Wind Speed, (e) Force E vs Wind Speed, and (f) Force F vs Wind Speed, at an angle of attack of 3.90°

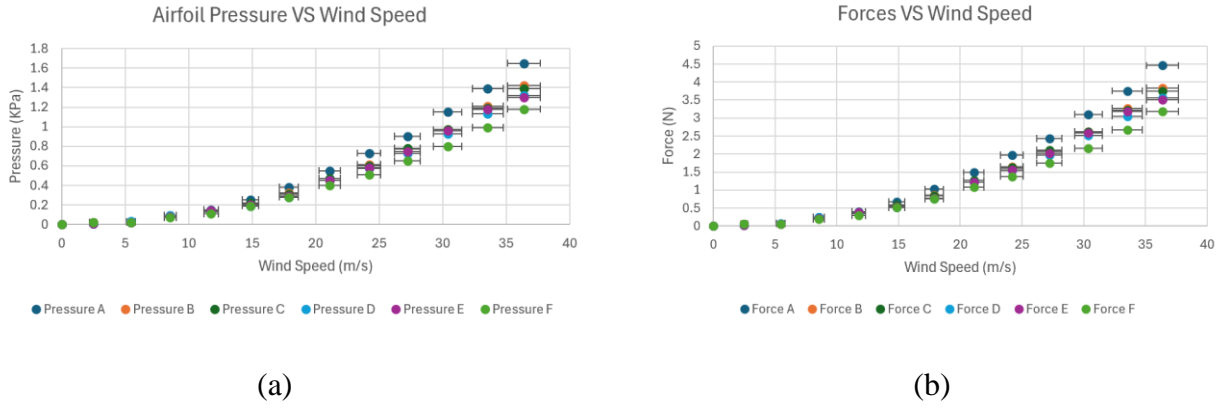


Figure 48. Corrected plots with linear and polynomial fit for (a) Airfoil Pressures vs Wind Speed and (b) Forces vs Wind Speed, at an angle of attack of 3.90°

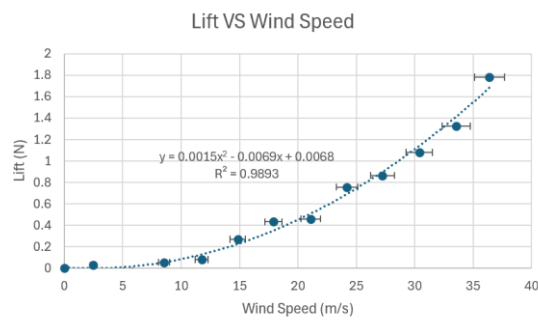


Figure 49. Corrected plot for Lift vs Wind speed with polynomial fit at 3.90° angle of attack

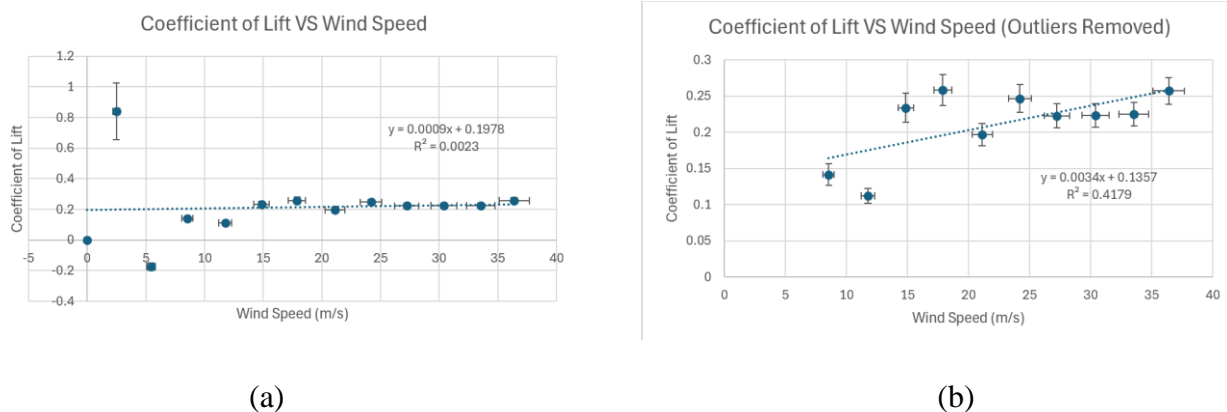


Figure 50. Corrected plot for Coefficient of Lift vs Wind Speed with a polynomial fit at 3.90° angle of attack (a) with outliers and (b) without outliers

D. Incorrect Lift Calculation Data for Trial 3 at 3.90° angle of attack

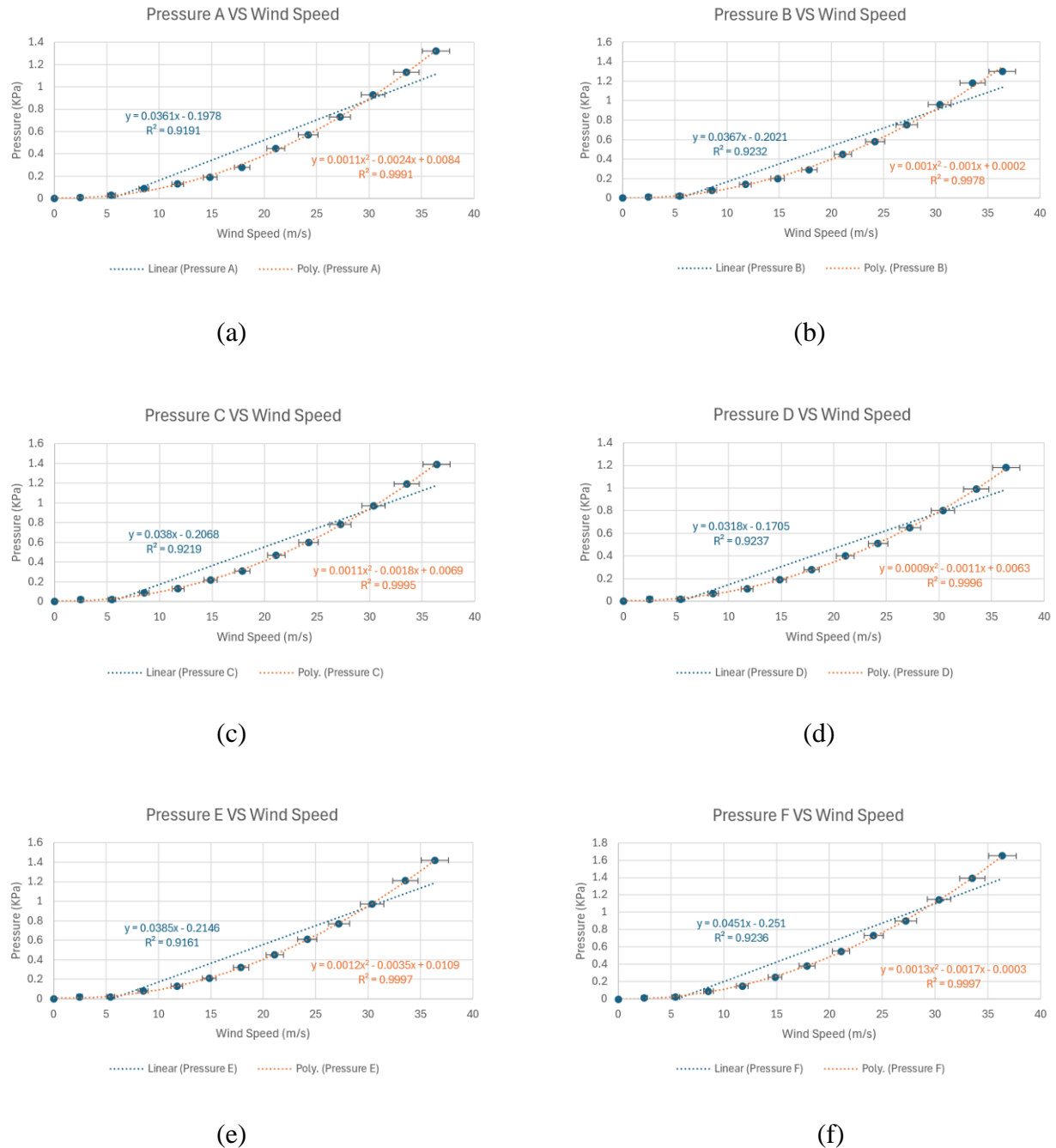


Figure 51. Incorrect plots for pressure measurements at varying wind speeds and with linear and polynomial fit for (a) Pressure A vs Wind Speed, (b) Pressure B vs Wind Speed, (c) Pressure C vs Wind Speed, (d) Pressure D vs Wind Speed, (e) Pressure E vs Wind Speed, and (f) Pressure F vs Wind Speed, at an angle of attack of 3.90°

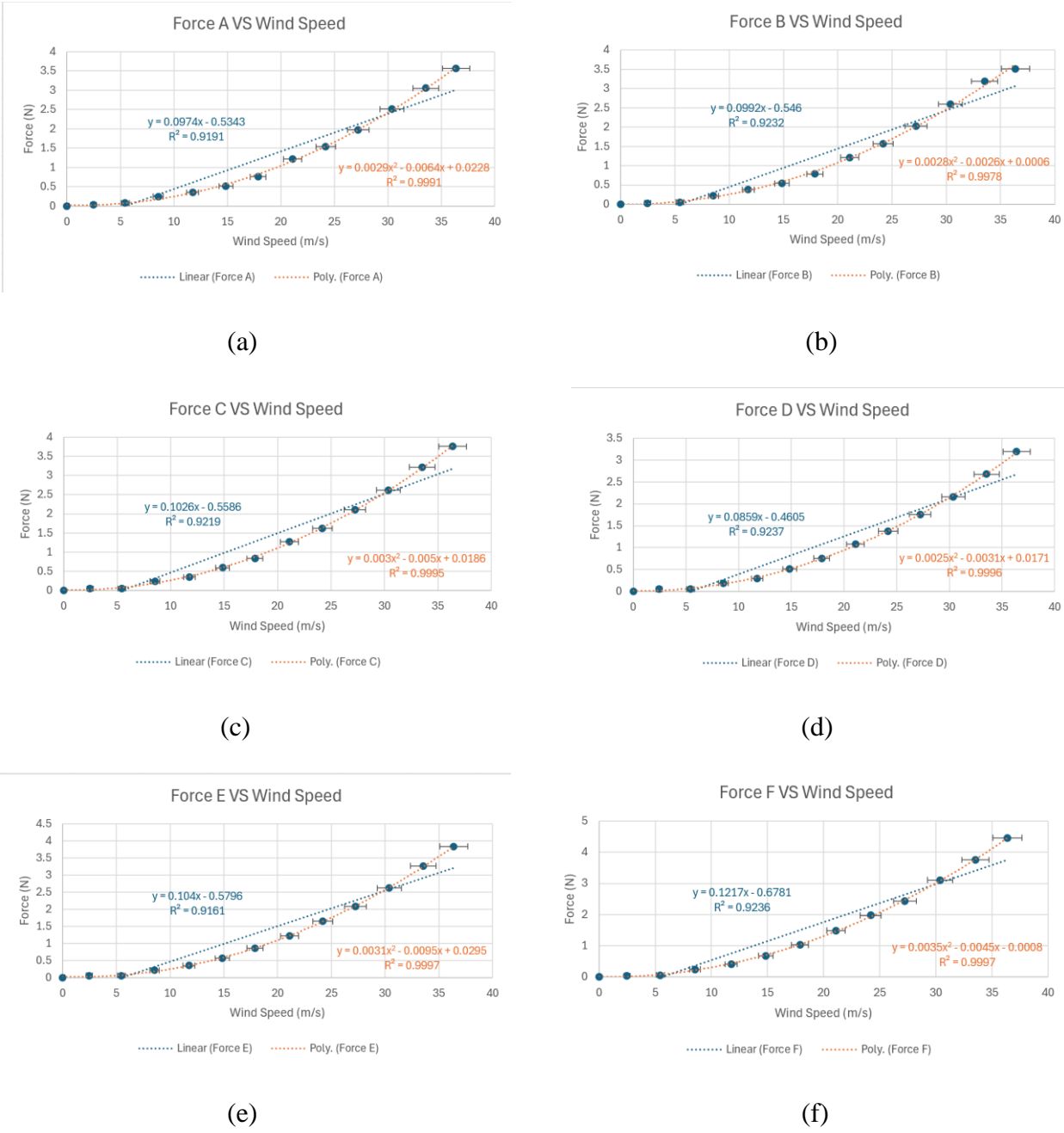


Figure 52. Incorrect plots for force measurements at varying wind speeds and with linear and polynomial fit for (a) Force A vs Wind Speed, (b) Force B vs Wind Speed, (c) Force C vs Wind Speed, (d) Force D vs Wind Speed, (e) Force E vs Wind Speed, and (f) Force F vs Wind Speed, at an angle of attack of 3.90°

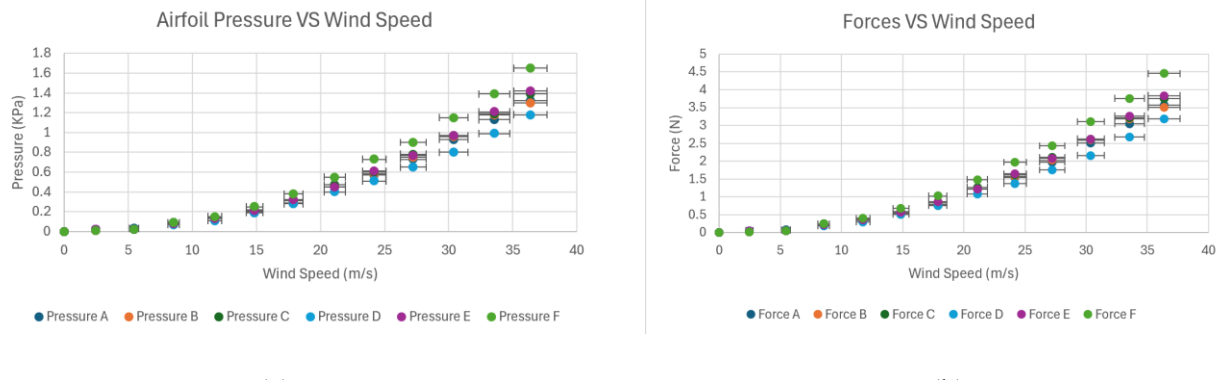


Figure 53. Incorrect plots with linear and polynomial fit for (a) Airfoil Pressures vs Wind Speed and (b) Forces vs Wind Speed, at an angle of attack of 3.90°

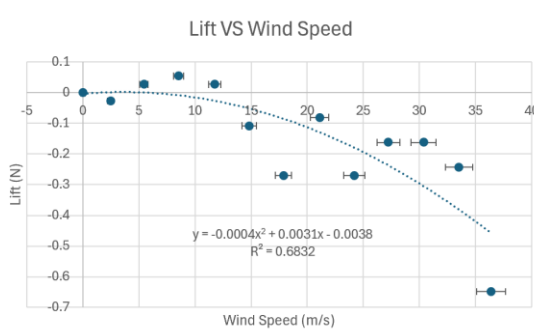


Figure 54. Incorrect plot for Lift vs Wind speed with polynomial fit at 3.90° angle of attack

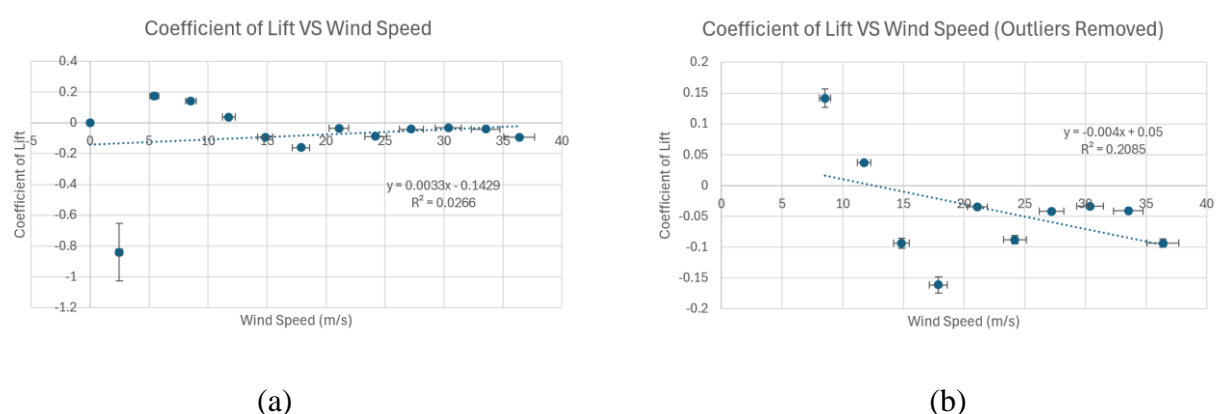


Figure 55. Incorrect plot for Coefficient of Lift vs Wind Speed with a polynomial fit at 3.90° angle of attack (a) with outliers and (b) without outliers

E. Lift Calculation Data for Trial 4 at 0° angle of attack and Dynamic Pressure of the Wind Tunnel

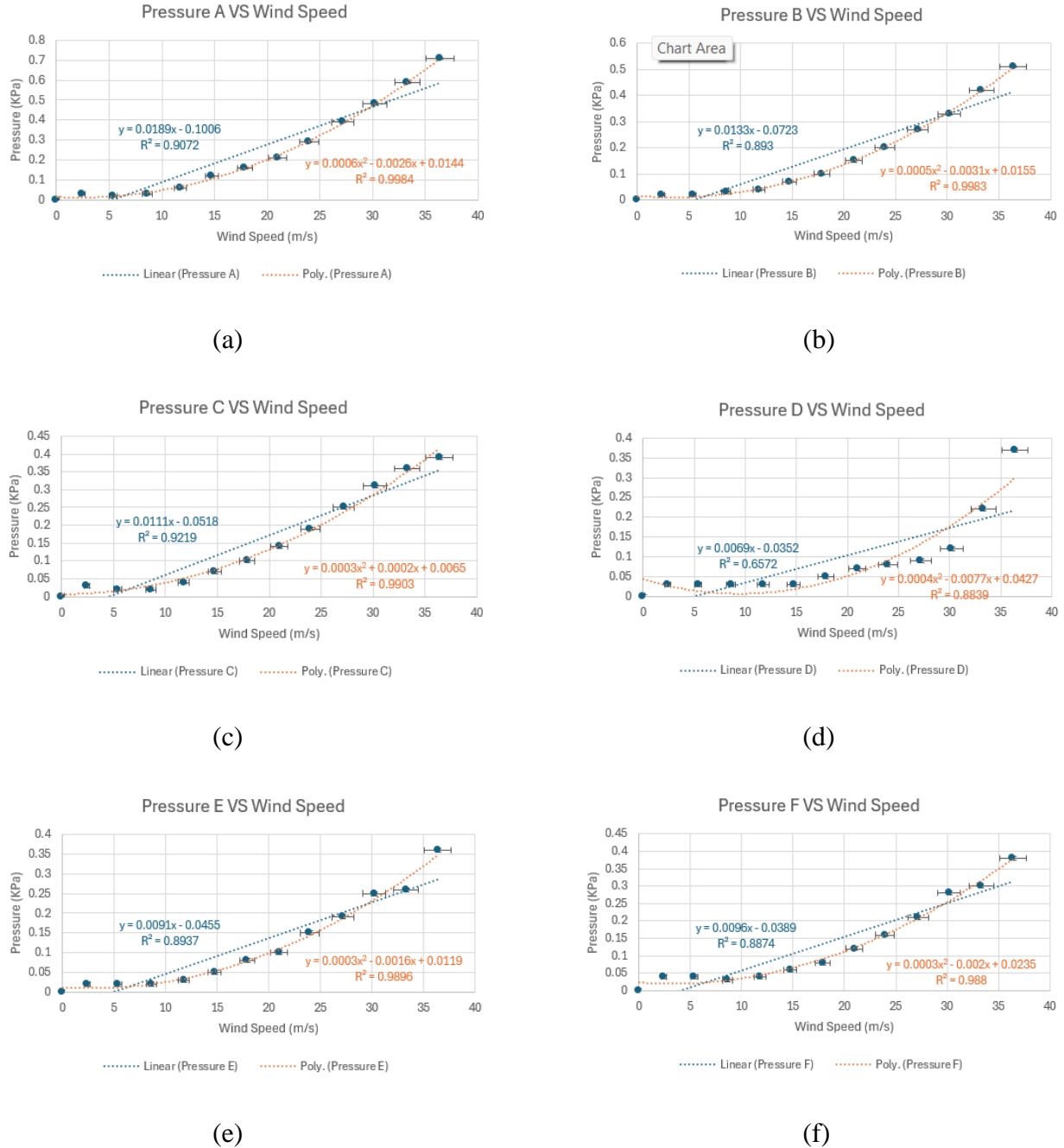


Figure 56. Plots for pressure measurements at varying wind speeds and with linear and polynomial fit for (a) Pressure A vs Wind Speed, (b) Pressure B vs Wind Speed, (c) Pressure C vs Wind Speed, (d) Pressure D vs Wind Speed, (e) Pressure E vs Wind Speed, and (f) Pressure F vs Wind Speed, at an angle of attack of 0° using wind tunnel pressure for the manometer setup

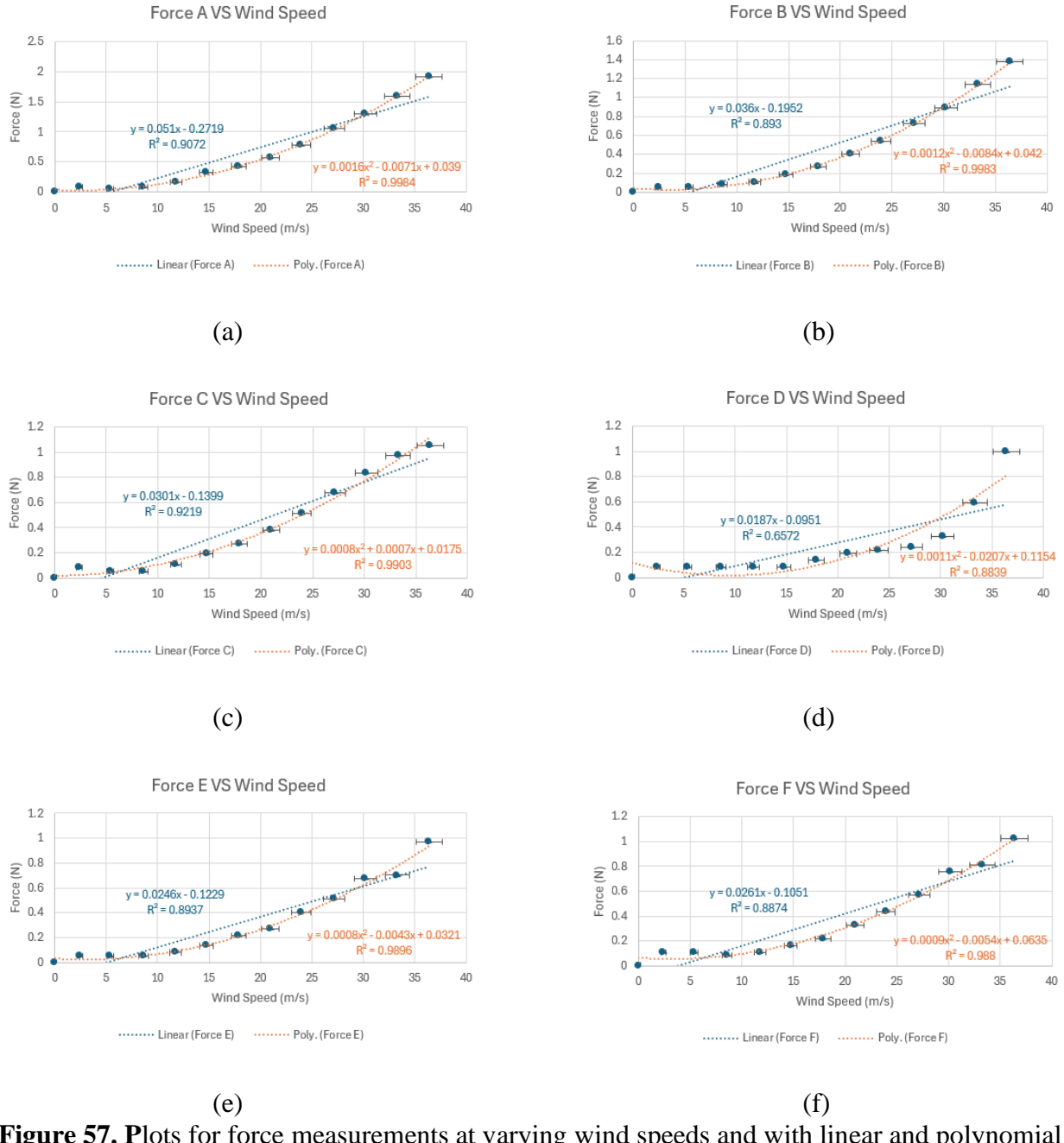


Figure 57. Plots for force measurements at varying wind speeds and with linear and polynomial fit for (a) Force A vs Wind Speed, (b) Force B vs Wind Speed, (c) Force C vs Wind Speed, (d) Force D vs Wind Speed, (e) Force E vs Wind Speed, and (f) Force F vs Wind Speed, at an angle of attack of 0° using wind tunnel pressure for the manometer setup.

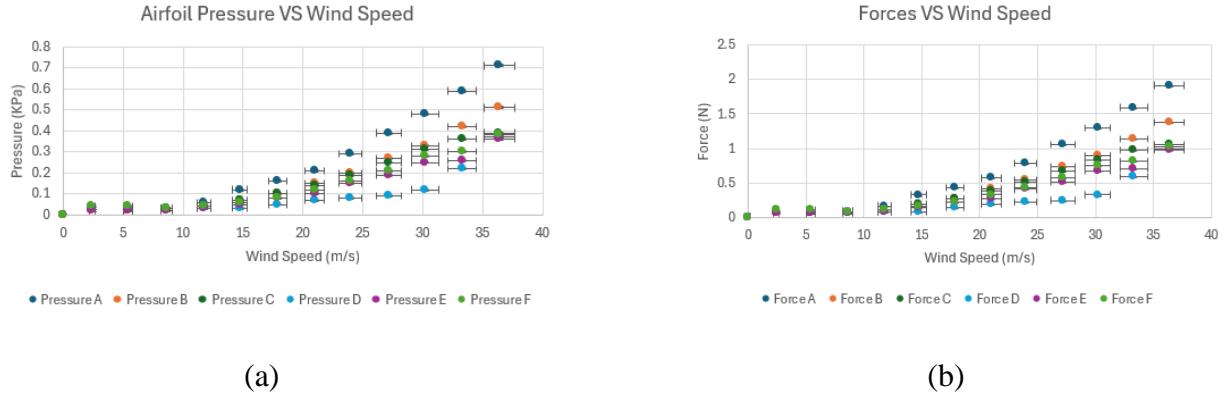


Figure 58. Plots with linear and polynomial fit for (a) Airfoil Pressures vs Wind Speed and (b) Forces vs Wind Speed, at an angle of attack of 0° using wind tunnel pressure for the manometer setup.

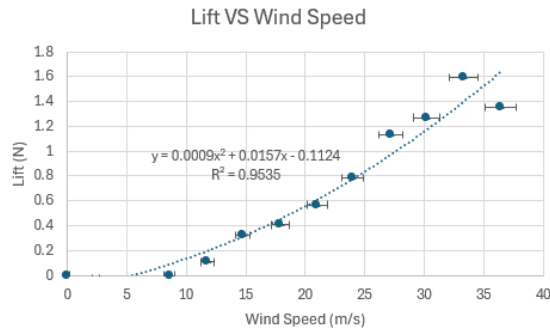


Figure 59. Plot for Lift vs Wind speed with polynomial fit at 0° angle of attack using windtunnel pressure for the manometer setup.

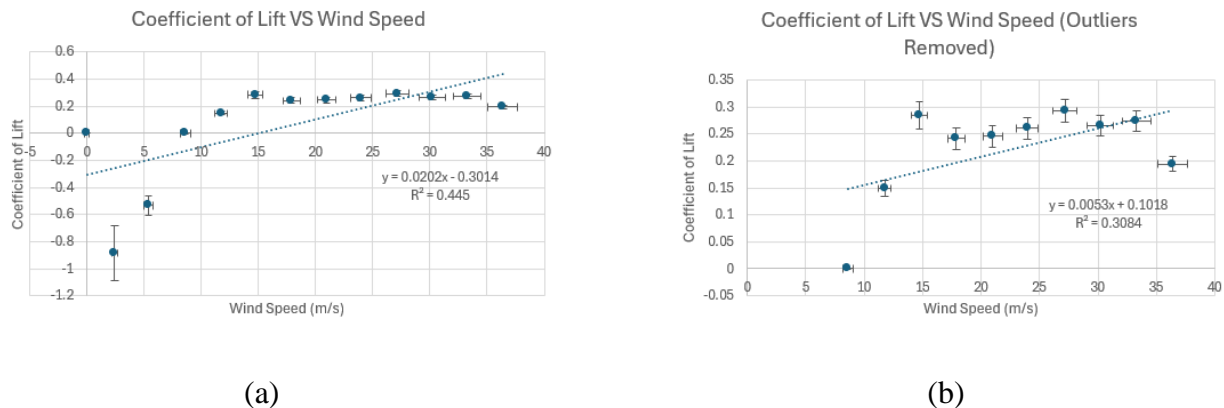


Figure 60. Plot for Coefficient of Lift vs Wind Speed with a polynomial fit at 0° angle of attack using wind tunnel pressure for the manometer setup (a) with outliers and (b) without outliers

F. Lift Calculation Data for Trial 5 at 10° angle of attack and Dynamic Pressure of the Wind Tunnel

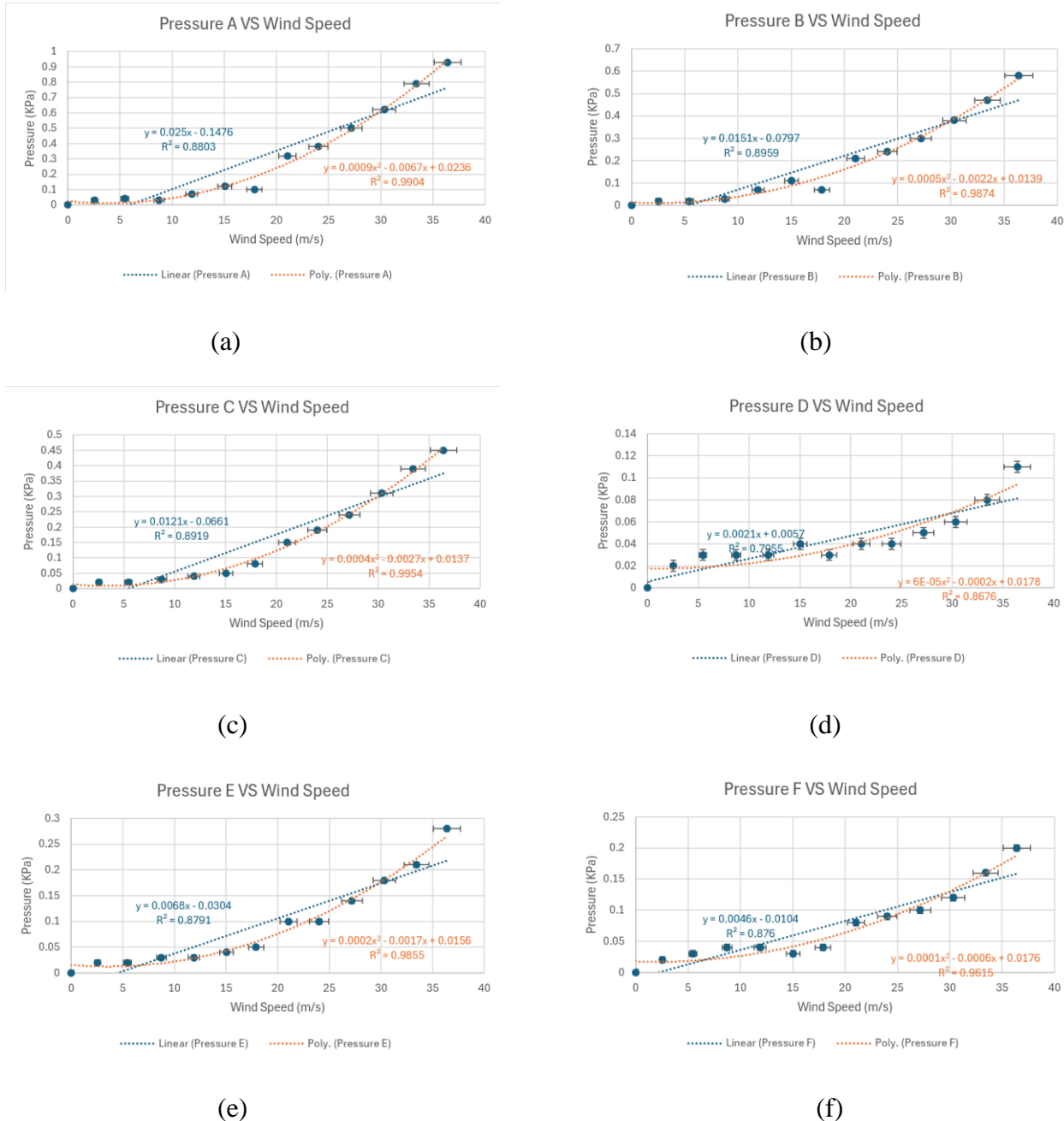


Figure 61. Plots for pressure measurements at varying wind speeds and with linear and polynomial fit for (a) Pressure A vs Wind Speed, (b) Pressure B vs Wind Speed, (c) Pressure C vs Wind Speed, (d) Pressure D vs Wind Speed, (e) Pressure E vs Wind Speed, and (f) Pressure F vs Wind Speed, at an angle of attack of 10° using wind tunnel pressure for the manometer setup

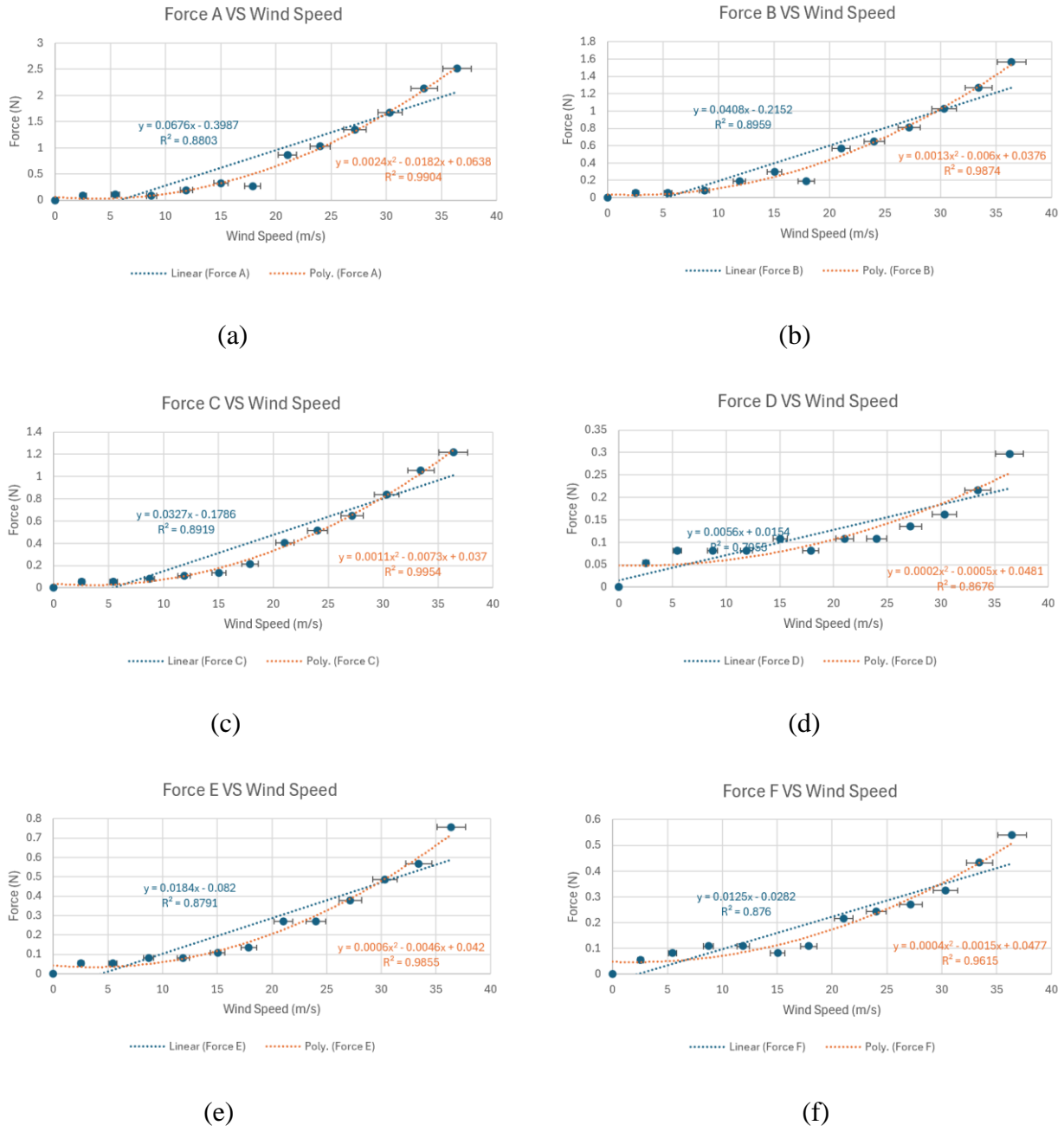


Figure 62. Plots for force measurements at varying wind speeds and with linear and polynomial fit for (a) Force A vs Wind Speed, (b) Force B vs Wind Speed, (c) Force C vs Wind Speed, (d) Force D vs Wind Speed, (e) Force E vs Wind Speed, and (f) Force F vs Wind Speed, at an angle of attack of 10° using wind tunnel pressure for the manometer setup.

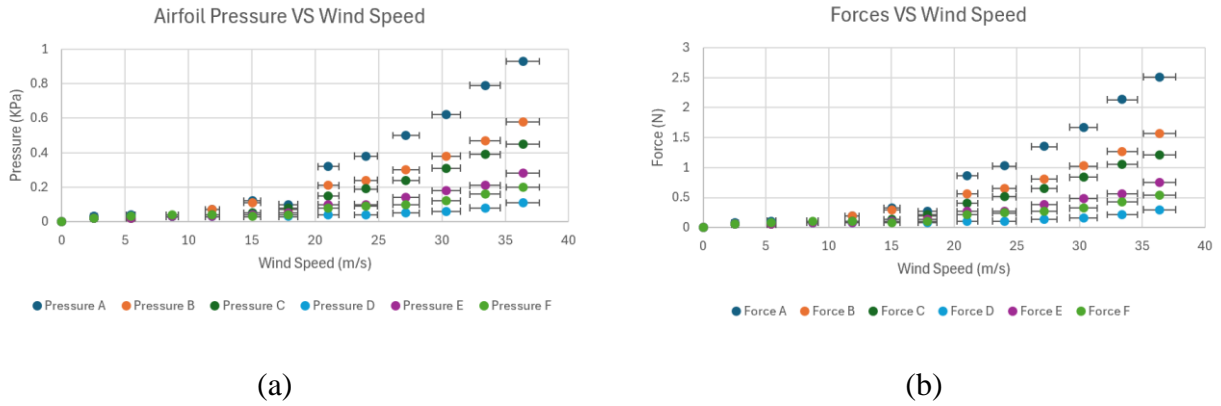


Figure 63. Plots with linear and polynomial fit for (a) Airfoil Pressures vs Wind Speed and (b) Forces vs Wind Speed, at an angle of attack of 10° using wind tunnel pressure for the manometer setup.

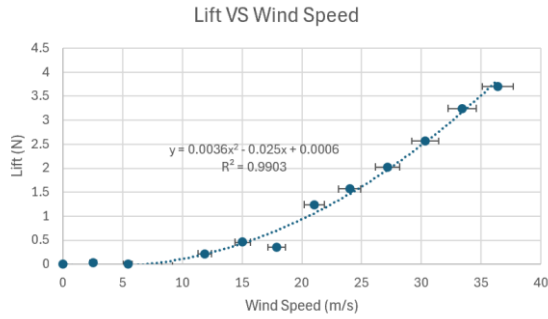


Figure 64. Plot for Lift vs Wind speed with polynomial fit at 10° angle of attack using wind tunnel pressure for the manometer setup.

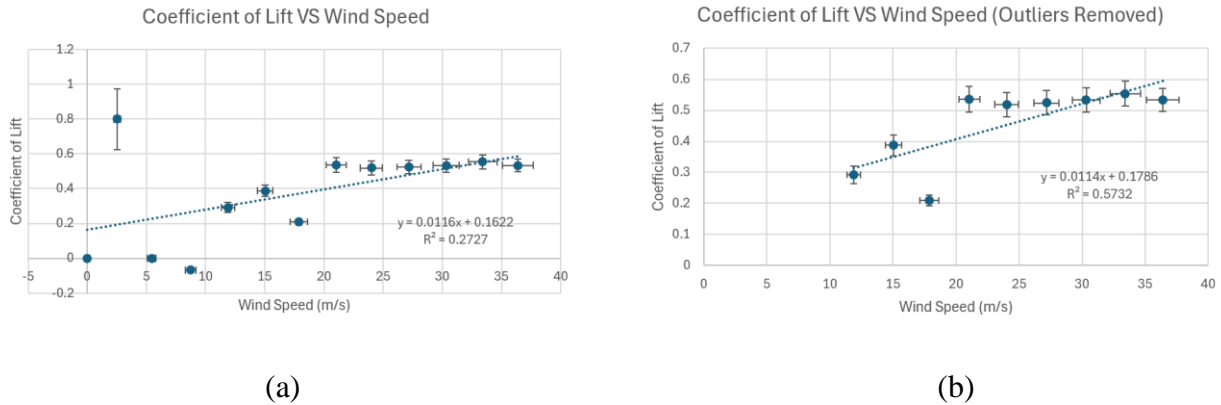


Figure 65. Plot for Coefficient of Lift vs Wind Speed with a polynomial fit at 10° angle of attack using wind tunnel pressure for the manometer setup (a) with outliers and (b) without outliers

Appendix VI: Theoretical Plots

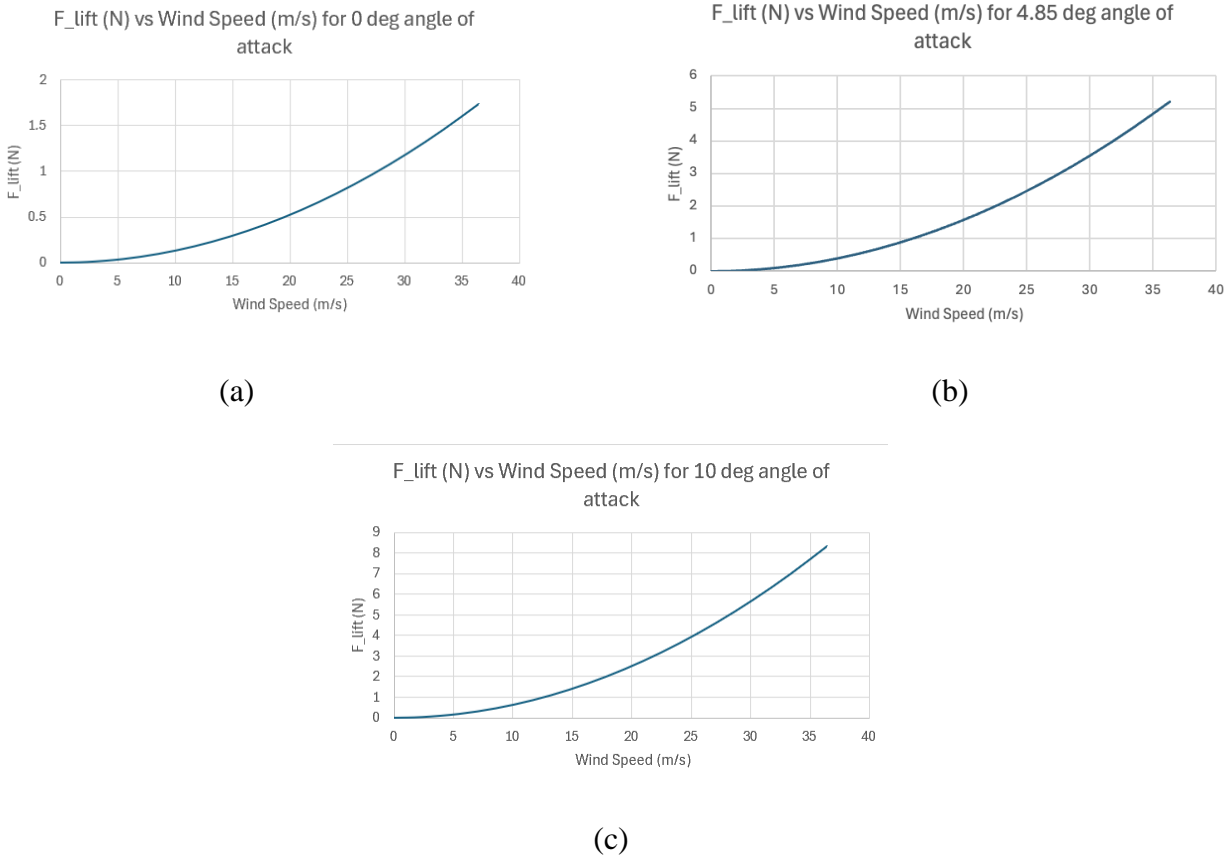


Figure 66. Theoretical Plots for F_{lift} vs Wind Speed for (a) 0° angle of attack, (b) 4.85° angle of attack and (c) 10° angle of attack